

## RESEARCH ARTICLE

10.1002/2017JB014620

## Key Points:

- We developed FEM of the 2015 Gorkha earthquake that accounts for variations in topography and material properties across the Himalayan arc
- Space geodetic observations reveal transient deformation following the Gorkha earthquake that is best explained by downdip afterslip
- Observed deformation is inconsistent with models of a low-viscosity (order of  $10^{18}$  Pa s or less) channel in the lower crust beneath Tibet

## Supporting Information:

- Supporting Information S1

## Correspondence to:

K. Wang,  
kjellywang@gmail.com

## Citation:

Wang, K., & Fialko, Y. (2018). Observations and modeling of coseismic and postseismic deformation due to the 2015  $M_w$  7.8 Gorkha (Nepal) earthquake. *Journal of Geophysical Research: Solid Earth*, 123, 761–779. <https://doi.org/10.1002/2017JB014620>

Received 27 JUN 2017

Accepted 7 DEC 2017

Accepted article online 13 DEC 2017

Published online 10 JAN 2018

## Observations and Modeling of Coseismic and Postseismic Deformation Due To the 2015 $M_w$ 7.8 Gorkha (Nepal) Earthquake

Kang Wang<sup>1</sup> and Yuri Fialko<sup>1</sup>

<sup>1</sup>Institute of Geophysics and Planetary Physics, Scripps Institution of Oceanography, University of California, San Diego, La Jolla, CA, USA

**Abstract** We use space geodetic data to investigate coseismic and postseismic deformation due to the 2015  $M_w$  7.8 Gorkha earthquake that occurred along the central Himalayan arc. Because the earthquake area is characterized by strong variations in surface relief and material properties, we developed finite element models that explicitly account for topography and 3-D elastic structure. We computed the line-of-sight displacement histories from three tracks of the Sentinel-1A/B Interferometric Synthetic Aperture Radar (InSAR) satellites, using persistent scatter method. InSAR observations reveal an uplift of up to  $\sim 70$  mm over  $\sim 20$  months after the main shock, concentrated primarily at the downdip edge of the ruptured asperity. GPS observations also show uplift, as well as southward movement in the epicentral area, qualitatively similar to the coseismic deformation pattern. Kinematic inversions of GPS and InSAR data and forward models of stress-driven creep suggest that the observed postseismic transient is dominated by afterslip on a downdip extension of the seismic rupture. A poroelastic rebound may have contributed to the observed uplift and southward motion, but the predicted surface displacements are small. We also tested a wide range of viscoelastic relaxation models, including 1-D and 3-D variations in the viscosity structure. Models of a low-viscosity channel previously invoked to explain the long-term uplift and variations in topography at the plateau margins predict opposite signs of horizontal and vertical displacements compared to those observed. Our results do not preclude a possibility of deep-seated viscoelastic response beneath southern Tibet with a characteristic relaxation time greater than the observation period (2 years).

### 1. Introduction

The 2015  $M_w$  7.8 Gorkha (Nepal) earthquake occurred along the central Himalayan arc, a convergent boundary between Indo-Australian and Eurasian plates. It was the largest seismic event along the Himalayan arc in the past 80 years, resulting in considerable human and economic losses. At present, the most active structure along the Himalayan range is the Main Frontal Thrust (MFT), the southernmost branch of the Main Himalaya Thrust (MHT) system, which absorbs about half of the total convergence rate of  $\sim 40$  mm/yr between India and Eurasia (Lavé & Avouac, 2000). GPS measurements made before the 2015 Gorkha earthquake suggest that the thrust is locked from its surface trace to  $\sim 100$  km to the north (Ader et al., 2012). Inversions of seismic and geodetic data showed that the 2015 Gorkha rupture did not reach the surface and that most of the moment release was concentrated in the deeper part of the seismogenic zone (between  $\sim 50$  and 100 km north of the MFT trace) (e.g., Fan & Shearer, 2015; Lindsey et al., 2015; Wang & Fialko, 2015). How the shallow portion of the MFT responds to stress changes induced by the 2015 Gorkha earthquake is important for assessing the future seismic hazard along the central Himalayan arc (Mencin et al., 2016; Wang & Fialko, 2015).

Previous models of the Gorkha event are mostly based on analytic or semianalytic solutions for dislocations in a homogeneous or layered elastic half-space (e.g., Elliott et al., 2016; Lindsey et al., 2015; Wang & Fialko, 2015; Whipple et al., 2016). The epicentral area of the 2015 Gorkha earthquake is characterized by strong variations in surface relief and material properties. The elevation above the sea level increases from a few hundred meters in the India plain to over  $\sim 5$  km in southern Tibet. Seismic topography studies reveal large changes in the crustal thickness and seismic velocities across the Himalayan range (e.g., Monsalve et al., 2008; Schulte-Pelkum et al., 2005). These lateral variations may introduce a bias in slip models based on assumptions

of a homogeneous or layered elastic half-space. More sophisticated models are also warranted by detailed high-quality space geodetic observations of coseismic deformation due to the 2015  $M_w$  7.8 earthquake, including data from the ALOS-2 and Sentinel-1 Interferometric Synthetic Aperture Radar (InSAR) missions, as well as the continuous Global Positioning System (GPS) network in Nepal (Ader et al., 2012; Elliott et al., 2016; Lindsey et al., 2015; Wang & Fialko, 2015).

Large earthquakes generate sudden stress changes in the ambient rocks that may activate a variety of time-dependent relaxation processes. Commonly considered models for postseismic deformation include viscoelastic relaxation in the lower crust and upper mantle, aseismic slip updip and/or downdip of the coseismic rupture, and poroelastic rebound in the fluid-saturated upper crust. If contributions of various relaxation mechanisms to the observed postseismic deformation can be identified and evaluated, they may provide valuable constraints on in situ mechanical properties of the host rocks. In particular, measurements of postseismic deformation following the 2015 Gorkha earthquake may provide insights into frictional properties of the MHT, effective viscosities of the lower crust and upper mantle beneath southern Tibet, and mechanisms of convergence and uplift in an active collision zone.

In this paper, we first refine the coseismic slip model of the 2015 Gorkha using finite element models (FEM) that explicitly account for lateral variations in material properties and surface topography across the Himalayan range. We then present the GPS and InSAR observations of postseismic deformation over  $\sim 2$  years after the Gorkha earthquake. We compare the observed postseismic deformation to models assuming various relaxation mechanisms (i.e., afterslip, viscoelastic relaxation, and poroelastic rebound) to explore what mechanism (or a combination of mechanisms) may have contributed to the early-stage postseismic deformation due to the 2015 Gorkha earthquake.

## 2. Coseismic Slip Models

### 2.1. Refinement of the Coseismic Slip Model With FEM

To account for lateral variations in surface topography and material properties, we use finite element models (FEM) to calculate surface displacements due to fault slip (Figure 1). FEM simulations are performed using Abaqus (Abaqus/Simulia, 2017). Slip on a fault is implemented using the split-node approach (e.g., Masterlark, 2003; Melosh & Raefsky, 1981) as follows: (1) The entire model domain is meshed in a way such that the two sides of the earthquake rupture have the same node distributions. (2) An extra (“dummy”) node is assigned to each node pair on a fault which shares the same coordinates. This dummy node does not belong to any finite element. (3) A linear constraint is defined for each node pair and the corresponding dummy node (see Figure S1 in the supporting information). (4) The nodes on both sides of the fault are then split by applying a displacement boundary condition along the direction of slip on a fault.

The fault geometry we adopted in our FEM simulations is based on one of the best fitting solutions of Wang and Fialko (2015). The strike and dip angles of the fault are  $285.4^\circ$  and  $7^\circ$ , respectively. The depth of the fault plane at the surface trace of the MFT is 4 km. Similar fault geometries were suggested by a number of studies of the 2015 Gorkha earthquake (e.g., Elliott et al., 2016; Grandin et al., 2015; Lindsey et al., 2015; Whipple et al., 2016). The dimension of our finite element model is 1,200 km  $\times$  1,200 km  $\times$  400 km along strike, dip, and vertical directions, respectively. To better resolve the displacement and stress fields close to the fault rupture, the element size gradually decreases toward the fault (Figure 1). The fault plane was discretized into  $\sim 3,000$  triangular elements the sizes of which gradually increase along the dip direction, with the smallest size of  $\sim 3$  km at the top edge of the fault plane. The model contains  $\sim 1.1$  million tetrahedron elements, with elements in the epicentral area as small as  $\sim 1$  km. We used the Shuttle Radar Topography Mission (SRTM) Digital Elevation Model (Farr & Kobrick, 2000) to incorporate topography into our finite element mesh. Vertical coordinates are referenced to the mean elevation south of the earthquake rupture (1.2 km above sea level). Unfortunately, no high-resolution seismic tomography model is available for the study area. As the most significant variations in geophysical (e.g., crustal thickness and seismic velocities) and geomorphologic (e.g., surface elevation) features in the study region occur in the longitudinal direction, we adopted a 2-D velocity structure derived from the regional seismic topography (Monsalve et al., 2008). Elastic moduli were calculated from  $P$  and  $S$  velocities assuming empirical relations between density and seismic velocities (Brocher, 2005). Below the depth of 70 km, material parameters are taken from the Preliminary Reference Earth Model (PREM). Figure 1b shows the assumed distribution of the Young’s modulus along the profile perpendicular to the MFT from the Indian plain to southern Tibet. Note that our FEM accounts not only for variations in elastic moduli with depth but also

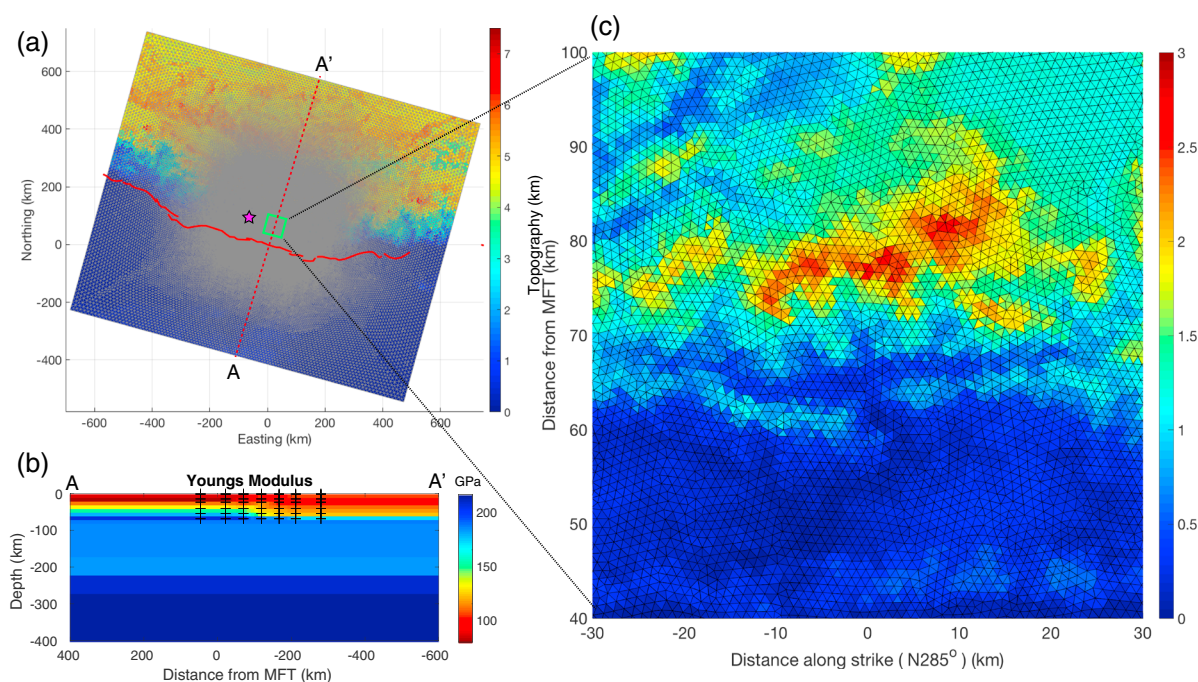


**Figure 1.** FEM mesh and elastic structure used in numerical simulations. (a) Map view of the model mesh. The mesh size gradually decreases toward the earthquake rupture. Colors denote surface topography, in kilometers. The red curve denotes the MFT trace. The magenta star denotes the epicenter of the 2015  $M_w$  7.8 Gorkha earthquake. (b) The Young's modulus variations along a profile normal to the MFT. The black crosses denote centers of resolution cells in the seismic tomography model of Monsalve et al. (2008). (c) Zoom-in of the FEM mesh in an area near the 2015 rupture (green box in Figure 1a).

for lateral variations in crustal thickness and material properties across the Himalayan range. We evaluated the effects of lateral variations in the elastic properties and topography on surface deformation by comparing surface displacements predicted by FEM simulations with homogeneous elastic half-space models (Wang & Fialko, 2015). Results of this comparison are shown in Figure 2. Differences between the analytic solutions and numerical (FEM) solutions assuming no topography and spatially uniform elastic moduli are within 20 mm or  $\sim 1\%$  for all three components of surface displacements (Figure 2, second row). These differences characterize the accuracy of numerical models. The effect of surface topography on the calculated surface displacements is up to  $\sim 50$  mm, in case of a homogeneous medium (Figure 2, third row). When both the surface topography and variations in material properties are included, the difference between the FEM and Okada's solutions is up to 0.2 m ( $>10\%$ ) for the vertical component of surface displacements (Figure 2, fourth row).

The Green functions calculated with FEM accounting for topography and spatial variations in material properties were used to invert for the coseismic slip distribution due to the 2015 Gorkha earthquake. We calculated the three components of surface displacements due to a unit slip along strike and dip directions on each node on a fault. Linear interpolation was used to calculate displacements at observation points that did not coincide with the mesh nodes at the surface. Surface displacement data and inversion parameters (relative weighting of different data sets, model smoothing, etc.) are the same as in Wang and Fialko (2015). Figure 3 shows a comparison of coseismic slip models based on FEM solutions assuming (a) homogeneous elastic properties and flat surface and (b) spatially variable elastic properties and surface topography (Figure 1). The two slip models are similar to each other, as well as to the dislocation model of Wang and Fialko (2015). The main difference is a somewhat larger slip amplitude in a model that accounts for topography and heterogeneity. The slip amplitude depends on the degree of smoothing applied in the inversions (a weaker smoothing yields a larger difference in slip amplitude). The two models shown in Figure 3 have similar posterior data fits, with the optimal value of smoothing determined by a trade-off between model roughness and data fit in each case. We find that for a wide range of smoothing parameters that yield reasonably good data fits, the model that takes into account material heterogeneity and surface topography always has a moderately larger ( $\sim 10\%$ ) slip amplitude compared to the reference (homogeneous flat) model.

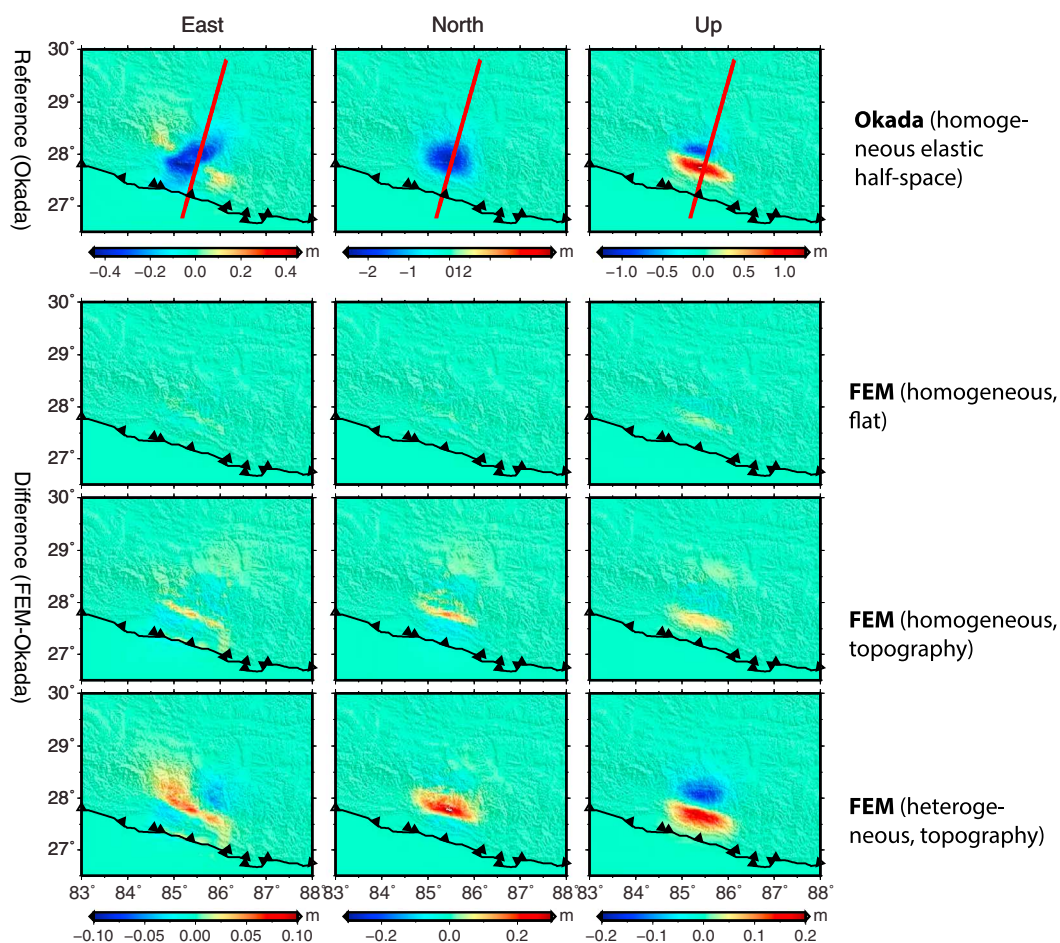


**Figure 2.** Forward calculations of coseismic surface displacements due to the 2015  $M_w$ 7.8 Gorkha earthquake. The coseismic slip model is from Wang and Fialko (2015). The elastic structure is from the seismic tomography model (Monsalve et al., 2008). (second to fourth rows) Differences in surface displacements between homogeneous half-space and FEM models. Surface displacements along a profile denoted by a red line are shown in supporting information Figure S2.

### 2.2. Coseismic Slip Model of the $M_w$ 7.3 Aftershock

The  $M_w$ 7.8 Gorkha earthquake was followed by a sequence of large ( $M_w > 5$ ) aftershocks. Most of these aftershocks occurred at the eastern end of the main shock rupture, including the largest ( $M_w$ 7.3) aftershock of 12 May 2015. The source parameters of the  $M_w$ 7.3 aftershock, including the hypocentral depth and fault attitude, are not well constrained. The estimated hypocentral depth of the  $M_w$ 7.3 aftershock is 15 km, almost twice as large as that of the main shock (8.3 km), although the main shock epicenter is farther away from the MFT trace (Figure 4). Some studies suggested that the main shock and the  $M_w$ 7.3 aftershock may have ruptured different faults (e.g., Feng et al., 2016). Because the  $M_w$ 7.3 aftershock likely plays a role in driving postseismic relaxation, and might help constrain the subsurface geometry of the MHT fault system, we performed inversions of surface deformation data for the coseismic slip model of the  $M_w$ 7.3 event. The data used in the inversions include line-of-sight (LOS) displacements derived from ALOS-2 InSAR data from the ascending track A156 (strip-mode) and the descending track D048 (ScanSAR mode). We did not use the C band data because of a poor phase correlation. The inversion procedure (data downsampling, calculation of Green functions, regularization, relative weighting between data sets, etc.) is the same as that used for the main shock (Wang & Fialko, 2015). We performed two sets of inversions to explore the fault geometries admissible by the data. In the first test (hereafter referred to as “test A”), we required the fault plane to go through the seismically determined hypocenter, while the dip angle of the fault was allowed to vary. In the second test (“test B”), we allowed both the hypocenter depth and fault dip to vary. The fault strike was fixed at  $285.4^\circ$  in all tests. Figure 4a shows the spatial relationship of the  $M_w$ 7.3 aftershock with the main shock. The aftershock occurred

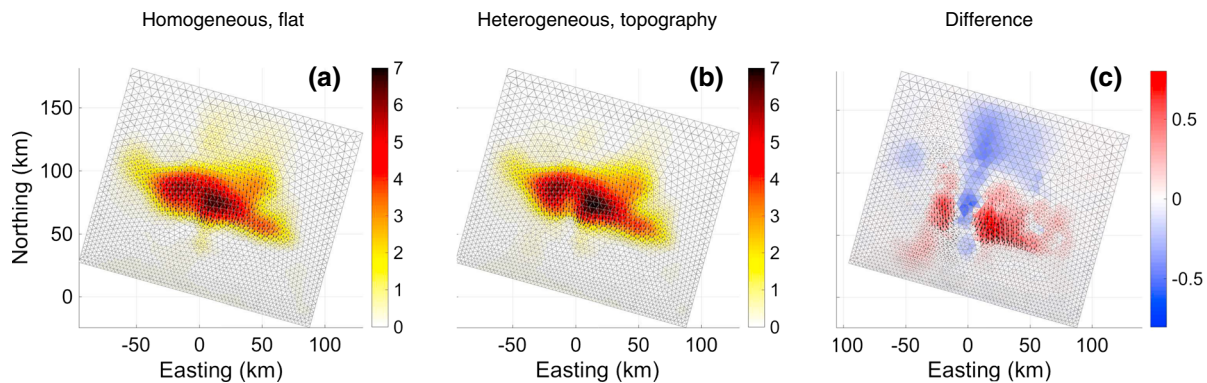


**Figure 3.** Comparison of coseismic slip models from inversions using FEM Green functions assuming (a) homogeneous elastic medium with no surface topography; (b) heterogeneous elastic structure from seismic tomography, with surface topography; and (c) the difference between Figures 3a and 3b. Slip is in the unit of meter.

at the periphery of coseismic rupture, effectively extending the latter farther to the east. Similar to the main shock, the  $M_w$ 7.3 aftershock was dominated by thrust motion with a small amount of dextral slip. The maximum slip close to the epicenter is  $\sim 4$  m, smaller than the value of  $\sim 6$  m estimated by Feng et al. (2016), although the inferred maximum slip depends on the degree of smoothing. The total moment release from the aftershock is  $8.1 \times 10^{19}$  N m, assuming the shear modulus of 33 GPa. The corresponding moment magnitude is  $M_w = 7.2$ , in reasonable agreement with the seismically determined value. Tests A and B revealed a trade-off between the rupture depth and dip: a deeper rupture would imply a steeper dip. Figure S3 quantifies this trade-off, and Figure S4 shows the model fit to the data. Given that the seismologic estimate of the hypocenter depth is subject to significant uncertainties, geodetic constraints on the geometry of the aftershock rupture unfortunately do not allow one to distinguish between a planar fault (Wang & Fialko, 2015; Whipple et al., 2016) and a ramp-and-flat structure (e.g., Avouac, 2007; Elliott et al., 2016). In any case, our results indicate that the  $M_w$ 7.3 aftershock likely occurred on the same fault as the main shock. Because a shallowly dipping planar fault results in a slightly better fit to the data for both the  $M_w$ 7.8 main shock and the  $M_w$ 7.3 aftershock, we use the respective geometry in all calculations below.

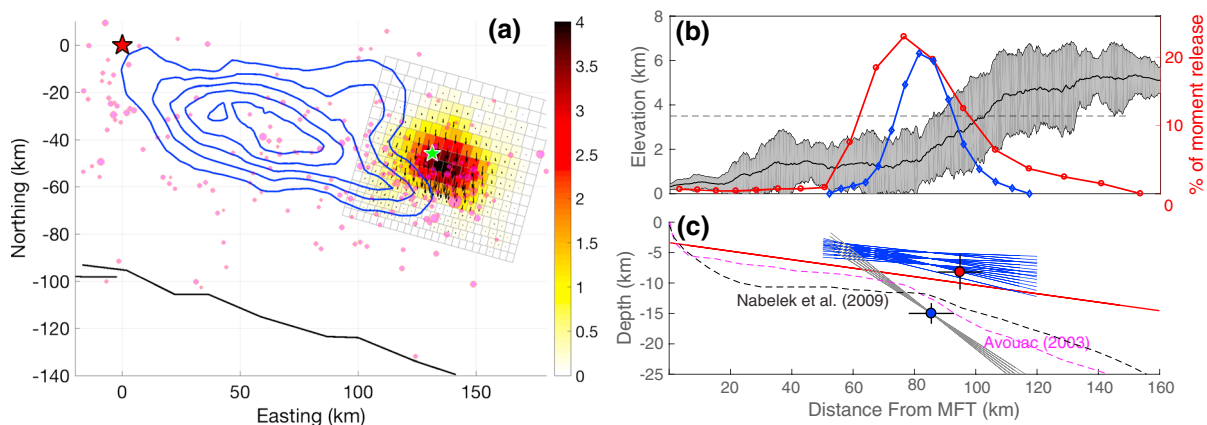


**Figure 4.** Coseismic slip model of the  $M_w$ 7.3 aftershock of 12 May 2015. (a) Map view illustrating spatial relationships between the main shock and the  $M_w$ 7.3 aftershock. Blue contours represent coseismic slip due to the main shock (1 m increments, starting from 1 m). Red and green stars denote the epicenters of the main shock and the  $M_w$ 7.3 aftershock, respectively. Black line represents the surface trace of the MFT. (b) Moment release of the main shock (red) and aftershock (blue), and surface topography (shaded gray) in the direction normal to the mean strike of the MFT (N285.4°) in the study area. (c) Cross-section view showing geometries of the best fitting fault models. Red line denotes the preferred main shock solution of Wang and Fialko (2015). Gray and blue lines denote admissible solutions for the aftershock (tests A and B, see the main text). Red and blue circles with error bars denote the USGS-determined hypocenters of the main shock and the  $M_w$ 7.3 aftershock, respectively. The dashed magenta and black lines denote the geometries of the MHT inferred by Avouac (2003) and Nabelek et al. (2009), respectively.

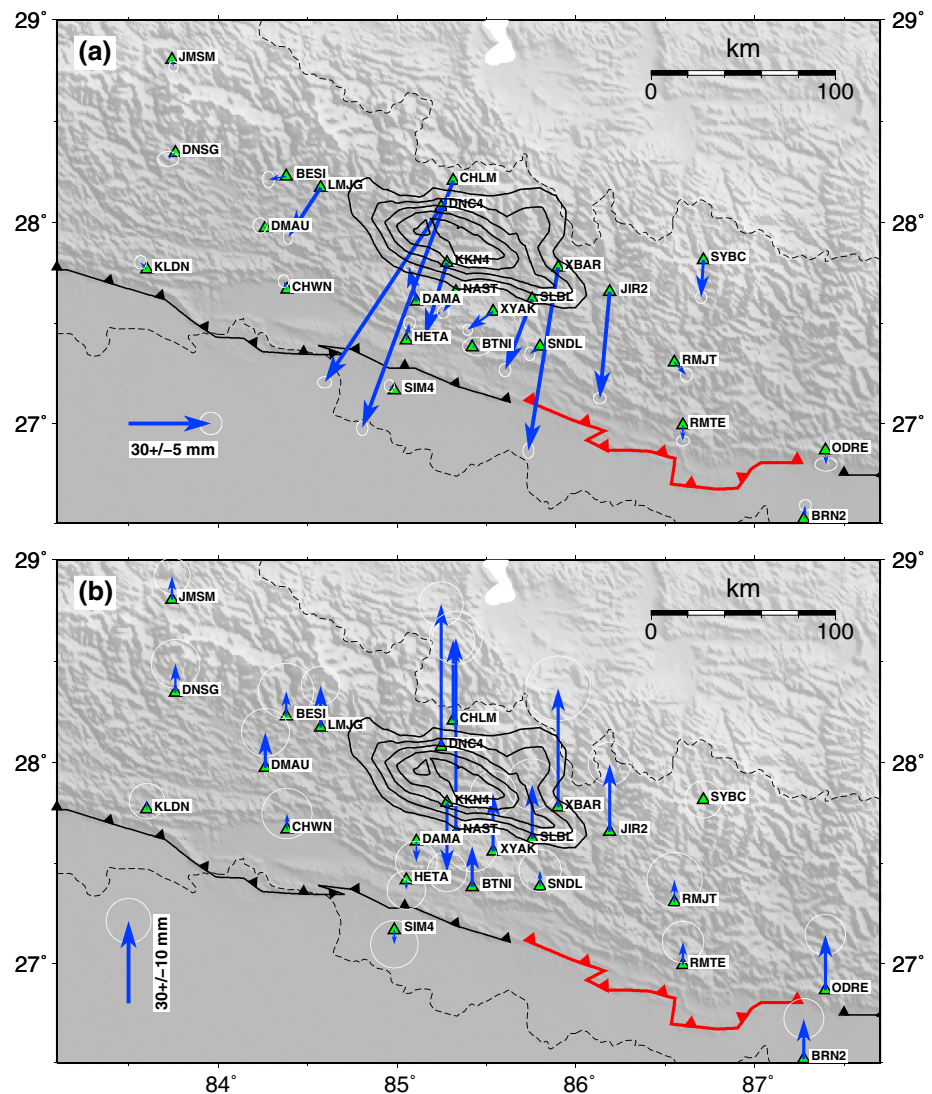


**Figure 5.** Cumulative postseismic GPS displacements due to the 2015 Gorkha earthquake ~2 years after the main shock: (a) horizontal component; (b) vertical component. The error ellipses represent the standard deviation of the difference between the observed time series and the logarithmic function (equation (2)) after correcting for the secular and seasonal variations. The black contours represent the coseismic slip at 1 m increments starting from 1 m. Lines with triangles represent the Main Frontal Thrust (MFT) in the study area. The section that was possibly ruptured during the 1933 Nepal-Bihar earthquake is marked in red. Only sites with postearthquake recordings spanning more than 300 days are shown.

### 3. Postseismic Deformation

#### 3.1. GPS Data

We used data from 32 continuous GPS (cGPS) sites within an area between 82–86°E and 26–30°N (Figure 5). The GPS network was deployed and operated under a collaboration between the California Institute of Technology (led by Jean-Philippe Avouac) and the Department of Mines and Geology of Nepal. Some sites were deployed by Roger Bilham, Rebecca Bendick, and David Mencin after the 2015 Gorkha earthquake. All the raw RINEX files are openly available at UNAVCO. We initially processed the raw GPS data using GAMIT/GLOBK (Herring et al., 2015). We compared the position time series with solutions from the Nevada Geodetic Laboratory (NGL) and found the two solutions to be in good agreement. As the NGL solutions are routinely updated, we decided to use them in this study.

The NGL data products include time series of station coordinates in the reference frame IGS08, as well as estimates of position changes due to the reference frame, interseismic deformation, seasonal variations

(e.g., due to hydrological loading), and the postseismic deformation following the 2015 Gorkha earthquake. In the Himalayan range, surface displacements caused by the annual hydrological loading are up to  $\sim 30$ – $50$  mm (Fu & Freymueller, 2012). The resulting deformation is found to be correlated with seasonal variations of seismicity (Bettinelli et al., 2008). Gravity Recovery and Climate Experiment (GRACE) mission provides monthly estimates of the regional mass change, which can be used to compute the surface deformation due to the terrestrial water storage change (e.g., Fu & Freymueller, 2012). While the surface deformation estimated using the GRACE data well matches the phase of seasonal variations in the GPS time series, the predicted amplitudes often differ from the observed ones by 30–50%, so the corrected GPS time series still exhibit a strong periodic component (Figure S4). We attempted to scale the predicted surface displacements to render the best fit with the raw GPS time series. We found, however, that this approach performs no better than simply fitting seasonal variations in the GPS time series with a sine/cosine function. Therefore, to isolate the contribution due to the postseismic deformation from other terms, we modeled the GPS position time series  $x(t)$  before the 2015 Gorkha earthquake as follows:

$$x(t) = p_1 + p_2 t + \sum_{i=1}^2 \left( p_{2i+1} \cos 2\pi \frac{t}{T/i} + p_{2i+2} \sin 2\pi \frac{t}{T/i} \right), \quad (1)$$

where  $p_1$  denotes the initial position at a certain reference time,  $p_2$  the secular velocity;  $T = 1$  year and  $i = 1, 2$  corresponds to annual and semiannual cycles (seasonal components), respectively. Some of the sites were deployed days to months after the 2015 Gorkha main shock. For those sites, we used parameters  $p_1$  to  $p_6$  estimated from the nearest cGPS sites which have sufficiently long ( $>500$  days) pre-earthquake recordings. We then subtracted the estimated secular and seasonal components (1) from the original time series to obtain time series  $y(t)$  that mainly reflect postseismic deformation due to the 2015 Gorkha earthquake. Here we assumed that the amplitude of seasonal signals does not change from year to year. Such an assumption was insufficient for some sites, as manifested by periodic variations in the residuals. We therefore visually checked time series  $y(t)$  after correcting for secular and seasonal contributions. If any periodic variations were still apparent in the time series  $y(t)$ , we approximated the residuals as follows:

$$y(t) = q_1 + q_2 \log_{10}(1 + t/\tau) + \sum_{i=1}^2 \left( q_{2i+1} \cos 2\pi \frac{t}{T/i} + q_{2i+2} \sin 2\pi \frac{t}{T/i} \right), \quad (2)$$

where  $\tau$  is a constant characterizing how fast the postseismic transients decay with time. Estimation of  $\tau$  is strongly affected by the early-epoch data. Depending on the dominant mechanism(s) involved in postseismic relaxation,  $\tau$  could vary spatially (e.g., Hetland & Hager, 2006; Rousset et al., 2012). Unfortunately, most of the GPS sites with high signal-to-noise ratio (SNR) used in this study do not have recordings immediately after the earthquake. We therefore assumed that the decay rate  $\tau$  is uniform throughout the GPS network and estimated it using the north component of the displacement time series at site CHLM, which has the largest SNR and almost continuous recordings during the entire observation period following the main shock. The estimated time constant  $\tau = 27 \pm 5$  days was used to refine secular and seasonal components at other sites, assuming that the postseismic deformation signal decays logarithmically (equation (2)). To avoid spurious fitting, we only used sites with postearthquake data spanning at least 300 days. We also corrected for offsets in the time series that might be due to equipment changes or local aftershocks. The resulting time series of the postseismic displacements at several GPS sites are shown in Figure S6.

Figure 5 shows the cumulative GPS displacements  $\sim 700$  days (from 26 April 2015 to 17 March 2017) after the 2015 Gorkha earthquake. Similar to the pattern of coseismic (Wang & Fialko, 2015) and early postseismic (Gualandi et al., 2016; Mencin et al., 2016) motion, most of the sites continued to move southward  $\sim 2$  years after the earthquake (Figure 5a). Displacements north of the rupture area are much larger compared to displacements south of the rupture. For instance, the north component of displacement at CHLM, a site just north of the main shock rupture, reaches up to  $\sim 90$  mm during the observation period, whereas displacements at sites located updip of the coseismic rupture (e.g., NAST, DAMA, HETA, and BTNI) are an order of magnitude smaller ( $<10$  mm). Most of the sites experienced a relative uplift after the Gorkha earthquake, with the exception of site KKN4 that subsided at a rate greater than the estimated uncertainties (Figure 5b). Some sites within the Kathmandu basin, e.g., NAST, show rapid ( $>100$  mm/yr) pre-earthquake subsidence, most likely due to water extraction. Because data shown in Figure 5b represent changes with respect to the preseismic rates (where available), a relative uplift at NAST is a result of slowing down of subsidence after the earthquake.

### 3.2. InSAR Data

The epicentral area of the 2015 Gorkha earthquake is well imaged by several SAR missions, in particular, Sentinel-1A/B and ALOS-2. The L band ALOS-2 data were instrumental for studies of coseismic deformation due to the Gorkha earthquake (e.g., Lindsey et al., 2015; Wang & Fialko, 2015). The use of ALOS-2 data for measurements of postseismic deformation is somewhat limited because of large revisit times, changes of acquisition modes, and strong ionospheric artifacts. We therefore primarily relied on the Sentinel-1A/B data in this study and used the ALOS-2 data to independently verify the results.

Because of the rugged topography, thick vegetation, and snow cover along the Himalayan front, the C band Sentinel-1 data suffer from phase decorrelation. To mitigate the correlation problem, we analyzed the Sentinel-1 data using the persistent scatter (PS) approach (Ferretti et al., 2001; Hooper et al., 2004). We first geometrically aligned the images to a single master and generated the corresponding master-to-slave interferograms with GMT5SAR (Sandwell et al., 2011; Xu et al., 2017). No filtering was applied at the stage of making the interferograms. The selection of persistent scatterers was performed with StaMPS version 3.3 (Hooper et al., 2007). Once the persistent scatterers are identified, the interferometric phase at the respective pixels can be computed between any given acquisition dates by combining the original master-to-slave pairs. We verified this procedure by checking the phase residuals in closed circuits of interferograms. We found that the phase residuals in any closed circuit are generally on the order of  $10^{-6}$  radians or less (Figure S7). This indicates good clock and orbital controls of the Sentinel-1 satellites. In total, we generated more than 200 interferograms for each of the three tracks covering the earthquake area (A085, D019, and D121). Interferograms were unwrapped individually to avoid a potential propagation of errors in the default “3-D unwrapping” procedure in StaMPS.

One of the most significant limitations to InSAR measurements of a low-amplitude deformation is the variability of water vapor in the atmosphere. The resulting atmospheric phase delays may consist of a stratified and a turbulent component (e.g., Ding et al., 2008; Parker et al., 2015; 2015). The stratified component is expected to spatially correlate with topography and exhibit systematic temporal (e.g., seasonal) variations. The turbulent component, on the other hand, is expected to be essentially random both spatially and temporally. In our study area, the topography varies from a few hundred meters in northern India to  $>5$  km in southern Tibet (Figure 1). Such significant variations in surface elevation are expected to produce significant atmospheric phase delays across the Himalayan range. Indeed, many interferograms show a strong correlation between the radar phase and topography. We applied a correction for the elevation-dependent humidity by performing a linear regression between the unwrapped radar phase and the digital elevation model. Data from the earthquake rupture area were excluded to prevent a possible contribution from surface deformation. We removed the best fitting linear dependence of the radar phase on topography from each interferogram. Interferograms were also “flattened” by subtracting the best fitting plane to account for possible orbital errors.

We next applied a correction for the turbulent part of atmospheric delays using CANDIS (Code for Atmospheric Noise Depression through Iterative Stacking) (Tymofeyeva & Fialko, 2015). The CANDIS algorithm exploits the fact that the radar phase of interferograms sharing a common acquisition contains the same contributions from atmospheric delays. The method applies if the deformation signal is linear or quasi-linear on a time scale that corresponds to a time span of an averaging stencil. An iterative procedure is used to improve estimates of atmospheric delays and deformation signals (Tymofeyeva & Fialko, 2015).

The residual radar phase corrected for the atmospheric delays is used to obtain the line-of-sight (LOS) displacement histories using the Small Baseline Subset (SBAS) method (e.g., Berardino et al., 2002; Tong & Schmidt, 2016). The initial rough estimate of the LOS displacement time series was obtained using a relatively strong smoothing in time. The estimated (quasi-linear) deformation signal was subtracted from the interferograms to update the atmospheric phase screens (APS). The updated APS were subtracted from the original interferograms, and the LOS displacement time series were recomputed with reduced temporal smoothing. The amount of smoothing was gradually reduced in each subsequent iteration to allow recovery of nonlinear signals. The iterations continued until convergence criteria were met. Figure 6 shows the postseismic LOS displacements for  $\sim 1.7$  years after the earthquake from three Sentinel-1 tracks covering the earthquake area. The LOS displacements from all three tracks show a region of decreases in radar range (an uplift, if the horizontal motion is ignored) at the downdip edge of the coseismic rupture. The maximum LOS displacements are up to  $\sim 70$  mm for both the ascending track A085 and the descending track D019 during the observation period. The LOS displacements from the descending track D121 are somewhat smaller, in part because of



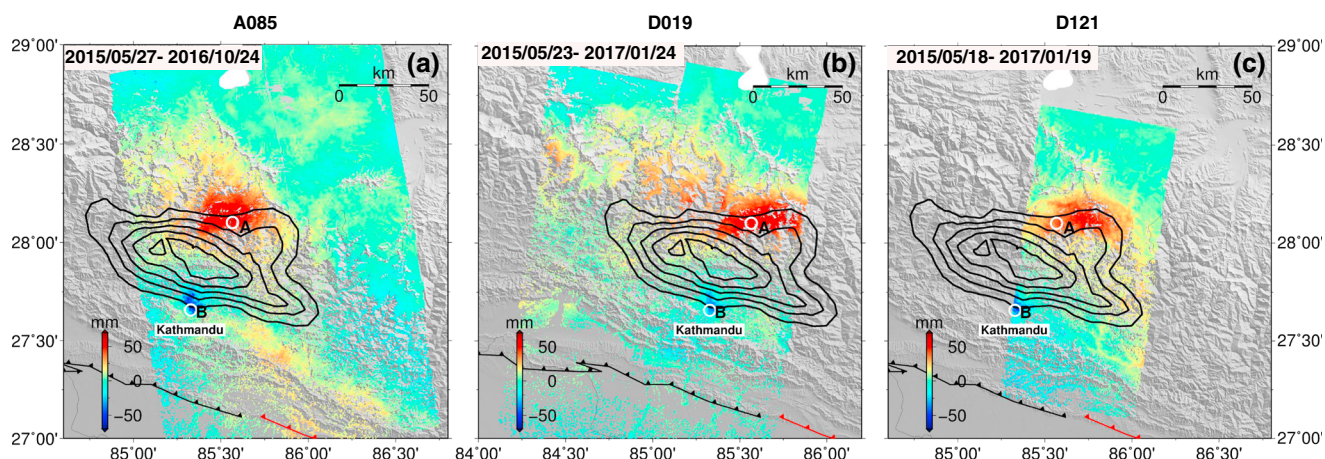


**Figure 6.** Postseismic LOS displacements from Sentinel-1 (a) ascending track A085, (b) descending track D019, and (c) descending track D121. Positive LOS displacements correspond to surface motion toward the satellite. Observation periods for each track are indicated in the top left corner of each panel. The time series of the LOS displacements at locations A and B indicated by white circles are shown in Figure 7.

differences in the radar incidence angle: the deformation anomaly is in the far range of track D121 but in the near range of tracks A085 and D019. A shallower incidence angle for track D121 reduces sensitivity to vertical motion. The positive LOS displacement anomaly seen in Figure 6 is indeed indicative of uplift, as (i) the same pattern is observed in data from the ascending and descending tracks, and (ii) the GPS data show that horizontal displacements are mainly in the north-south direction (Figure 5a), which has only a small component in the satellite line of sight. The LOS displacements also reveal subsidence in the Kathmandu basin, likely due to water pumping in the city of Kathmandu. We used ALOS-2 data to independently verify results of our analysis of Sentinel-1 data. We computed average LOS velocities from several ALOS-2 interferograms from track D048 (Figure S8a). While the velocities are noisier because of a relatively small number of radar acquisitions, the main features seen in Sentinel-1 data (Figure 6) are also present in the average LOS velocities derived from ALOS-2 data (Figure S8b). Figure 7 shows the time series of LOS displacements derived from Sentinel-1 data in the regions of anomalous deformation: site A is in the area of positive LOS displacements, and site B is in the area of negative LOS displacements, close to the cGPS site NAST. Although a relatively strong smoothing was applied in the SBAS time series analysis, the LOS displacements at site A clearly show a decaying signal, consistent with what one would expect from a postseismic transient. Given that data from the three Sentinel-1 tracks used in this study were acquired on different dates, similarities in both spatial (Figure 6) and temporal (Figure 7) patterns of surface deformation suggest that the results are robust. We also performed a number of sensitivity tests in which only a subset of interferograms was used to compute the displacement time series. Results were similar to those shown in Figures 6 and 7. Finally, a comparison of InSAR time series with cGPS data from site NAST shows a reasonable agreement (Figure 7b). The LOS velocities derived from the InSAR time series analysis are somewhat smaller than the GPS velocity; this may be due to averaging of the InSAR data over a finite area around the cGPS site.

#### 4. Modeling of Postseismic Deformation

In this section we evaluate predictions of models of postseismic deformation due to various relaxation mechanisms and compare them to InSAR and GPS data to investigate which mechanism (or a combination of mechanisms) may have contributed to the observed postseismic deformation over a period of  $\sim 2$  years following the 2015 Gorkha earthquake. We focus on end-member models that consider contributions of each mechanism (afterslip, viscoelastic relaxation, and poroelastic rebound) to the observed surface motion. Implications for concurrent relaxation processes are considered in section 5.

##### 4.1. Viscoelastic Relaxation

We compute surface displacements due to viscoelastic relaxation using the same finite element model that was used in the inversions for coseismic fault slip (section 2.1). To validate the FEM results, we compared surface displacements predicted by the finite element model to semianalytic solutions (Wang et al., 2006), using the same coseismic slip model and rheologic structure. In particular, we assumed a 1-D layered structure

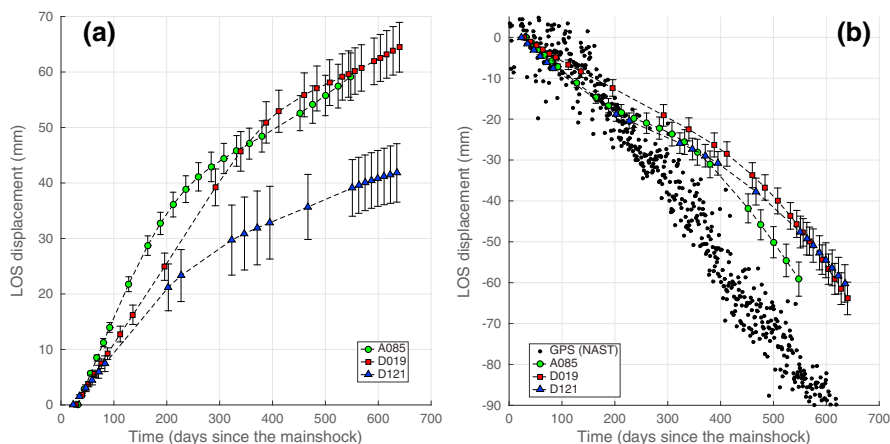


**Figure 7.** LOS displacement time series at (a) site A in the area of positive LOS displacements at the downdip end of the coseismic rupture; (b) site B in the area of negative LOS displacements near the cGPS site NAST (Kathmandu basin). The error bars represent the standard deviation of the LOS displacements for persistent scatters (PS) within a circle of 500 m radius. The GPS displacements are projected on the LOS of the ascending track A085.

with a 20 km thick elastic layer underlain by a viscoelastic half-space with the dynamic viscosity of  $10^{18}$  Pa s. Figures 8a and 8b show the surface displacements due to viscoelastic relaxation 500 days after the earthquake calculated using the two methods. The model predictions are in excellent agreement, indicating that our numerical model is sufficiently accurate. Both models show pronounced subsidence and northward motion (up to  $\sim 0.4$  m) in the epicentral area, opposite to the sense of the observed displacements (Figures 5 and 6).

To account for possible lateral variations in rheologic properties across the Himalayan front (e.g., Clark & Royden, 2000; Huang et al., 2014; Royden et al., 1997), we considered a suite of models in which the lower crust beneath the Tibetan Plateau includes a layer with reduced viscosity (Figure 9). In these models, we assumed that the entire 50 km thick crust of the Indian plate is elastic and that the upper mantle below both India and southern Tibet is viscoelastic with the dynamic viscosity of  $10^{20}$  Pa s. We considered a range of viscosities of the lower crust of southern Tibet  $\eta_T$ , as well as distances from the MFT trace,  $L_T$ , at which the transition to viscosity  $\eta_T$  occurs.

Figure 10 shows the predicted surface displacements due to viscoelastic relaxation for a laterally heterogeneous rheologic structure with  $L_T = 120$  km and  $\eta_T = 10^{18}$  Pa s. Similar to a model that assumes a 1-D layered rheologic structure (Figure 8), the heterogeneous model also predicts northward motion and subsidence in the epicentral area, opposite to the observed pattern. The predicted InSAR range changes (Figure 11) are also

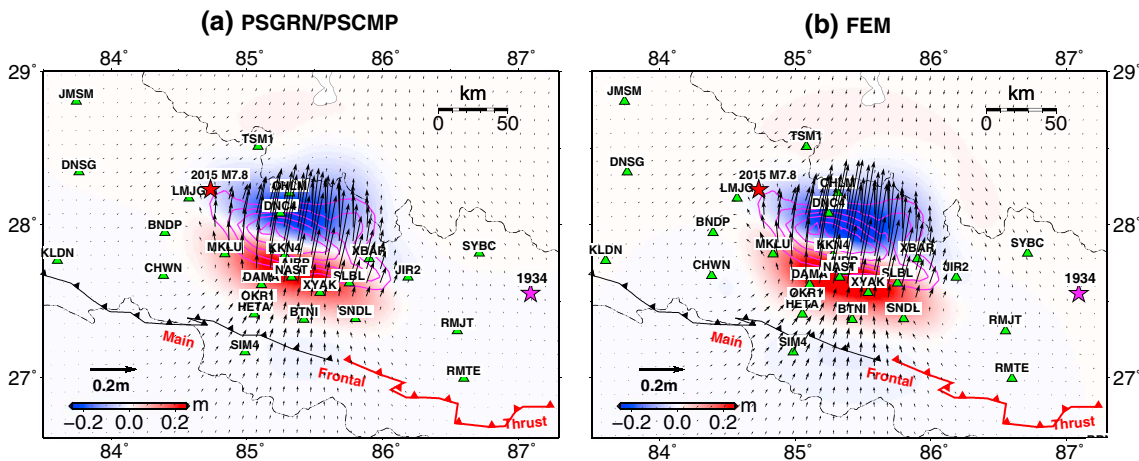


**Figure 8.** Predicted surface displacements due to viscoelastic relaxation 500 days after the 2015 Gorkha earthquake, assuming a 20 km thick elastic upper crust, and viscoelastic lower crust and upper mantle with the dynamic viscosity of  $10^{18}$  Pa s. Results obtained using (a) PSGRN/PSCMP (Wang et al., 2006), and (b) FEM simulations. Color represents the vertical motion. Green triangles denote the GPS stations used in this study.

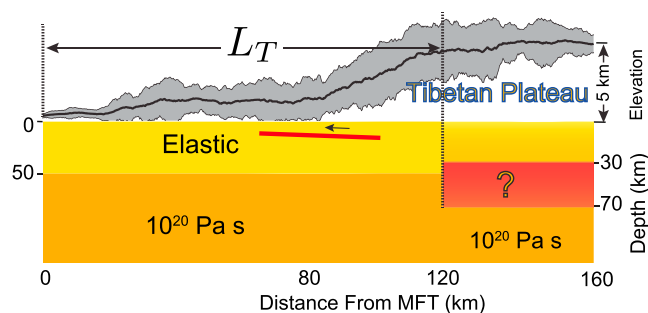


**Figure 9.** Model setup for the heterogeneous rheologic structure of the lithosphere across Himalaya. Red solid line denotes the 2015 Gorkha earthquake rupture. A lateral transition in rheology of the lower crust occurs at a distance  $L_T$  from the MFT surface trace. The entire 50 km thick Indian crust and the top 30 km of the Tibetan crust are assumed to be elastic. The upper mantle beneath both the Indian plate and southern Tibet is assumed to be viscoelastic with an effective viscosity of  $10^{20}$  Pa s.

opposite to the observed range changes (Figure 6). The modeled northward displacements at some of the GPS sites are up to  $\sim 50$  mm 2 years after the event. The surface displacements in case of the laterally heterogeneous model are generally smaller than those predicted by the 1-D layered model. This is because in the heterogeneous model, the region that undergoes relaxation is farther away from the earthquake rupture. The amplitude of surface displacements decreases for a larger  $L_T$ . All results below correspond to  $L_T = 120$  km (the distance from the MFT trace beyond which the Tibetan Plateau reaches its average elevation of more than 4 km above the sea level, Figure 9).

Other variables explored in our forward models include different thicknesses and depths of the low-viscosity layer beneath southern Tibet and different viscosity contrasts across the Himalayan range. None of the tested models produced a sense of motion consistent with the GPS and InSAR observations. We therefore conclude that viscoelastic relaxation was not the dominant mechanism of postseismic deformation in the first  $\sim 2$  years following the Gorkha earthquake, at least in the

near-to-intermediate field (within  $\sim 150$  km from the earthquake rupture). Models including a low-viscosity layer in the lower crust beneath Tibet do predict southward motion in the far field, in particular north of the  $29^\circ\text{N}$  latitude (Figure 10). Measurements of the surface deformation over a broader area may provide further constraints on the effective rheology of the lower crust and upper mantle beneath southern Tibet.

#### 4.2. Poroelastic Rebound

We evaluated potential contributions due to poroelastic rebound by differencing models of coseismic displacements under drained and undrained conditions. We assumed that the poroelastic rebound is confined to the top 20 km of the crust and the drained and undrained values of the Poisson's ratio of 0.25 and 0.28, respectively. The coseismic slip model of Wang and Fialko (2015) was used in this calculation. Figure 12 shows the predicted surface displacements due to the poroelastic rebound. Overall, the poroelastic rebound model does predict the southward motion and uplift south of the downdip edge of the coseismic rupture, qualitatively consistent with the GPS and InSAR measurements. However, the displacements predicted by the poroelastic rebound are much smaller ( $< 10$  mm) than the observed displacements. Increasing the difference between the drained and undrained values of the Poisson's ratio can amplify the displacement magnitude but less than by a factor of 2 for reasonable values of poroelastic material parameters. Smaller assumed values of the thickness of the fluid-saturated layer would decrease the magnitude of predicted surface displacements. We conclude that while the poroelastic rebound may have contributed to the observed deformation transient, its contribution is relatively small. Similar conclusions were reached in several previous studies of large shallow earthquakes (e.g., Barbot et al., 2008; Gonzalez-Ortega et al., 2014).

#### 4.3. Afterslip

##### 4.3.1. Kinematic Inversions

An overall similarity between patterns of coseismic and postseismic displacements (southward motion and uplift) documented by space geodetic observations is suggestive of a continued slip on a fault that produced the earthquake. To get an insight into the spatial distribution of afterslip, we performed kinematic inversions of the observed surface displacements. We assumed that afterslip occurred on the same fault plane as the coseismic rupture. We used the fault geometry based on the coseismic slip model of Wang and Fialko (2015), extended both in strike and dip directions. We assumed that the fault has a dip angle of  $7^\circ$  and the depth of the fault plane at the surface trace of the MFT is 4 km. We calculated the Green functions using analytic solutions for a dislocation in a homogeneous elastic half-space (Okada, 1985).

Both the GPS and InSAR data were used in the inversions. For the GPS data, we used the horizontal components of the cumulative displacements as

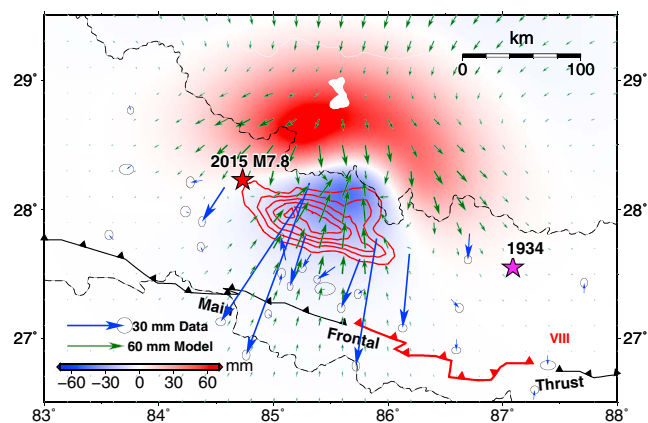


**Figure 10.** Predicted surface displacements due to viscoelastic relaxation for a heterogeneous rheologic structure with  $L_T=120$  km and  $\eta_T = 10^{18}$  Pa s (see Figure 9). Color represents vertical displacements.

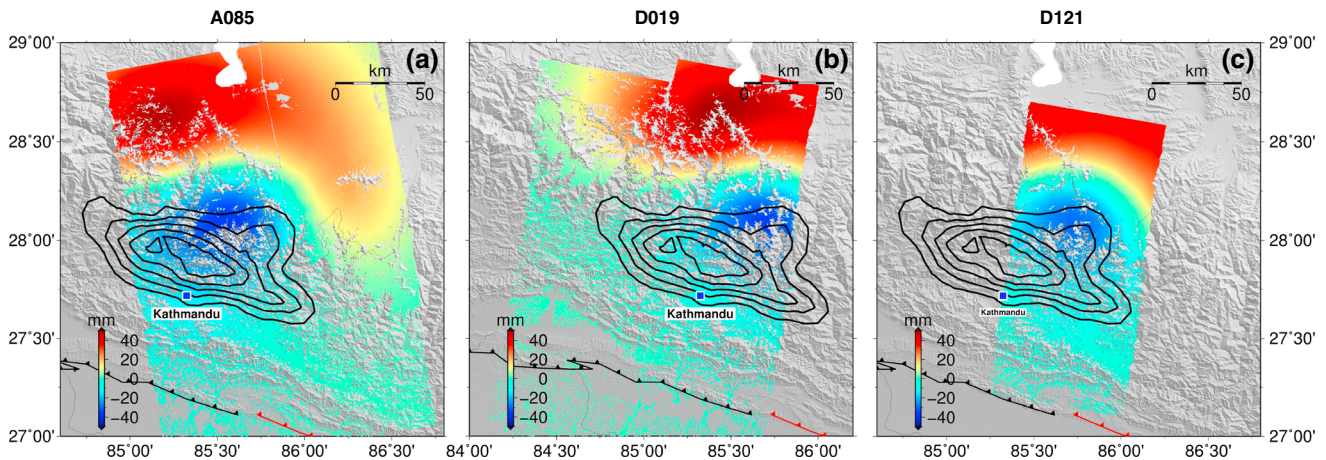


**Figure 11.** Predicted InSAR LOS displacements due to viscoelastic relaxation for a heterogeneous rheologic structure with  $L_T=120$  km and  $\eta_T = 10^{18}$  Pa s (see Figure 9).

shown in Figure 5a. InSAR observations were made over somewhat different time periods. To ensure consistency between the two data sets, we scaled the LOS displacements shown in Figure 6 by a factor  $F$  that accounts for the InSAR time span for each track, assuming that the LOS displacement histories follow the same logarithmic function (time constant  $\tau$  of 27 days) that best fits the GPS time series,

$$F = \frac{\log(1 + t_{gps}/\tau)}{\log(1 + t_2/\tau) - \log(1 + t_1/\tau)}, \quad (3)$$

where  $t_{gps}$  is the duration of the GPS time series (starting immediately after the earthquake), and  $t_1$  and  $t_2$  are the start and the end times of the respective InSAR time series.

The InSAR data were downsampled iteratively during the inversion using the current best fitting model to avoid oversampling in areas with large phase gradients due to noise (atmospheric perturbations, unwrapping errors, etc.) (Wang & Fialko, 2015). To investigate the model sensitivity to different data sets, we inverted the GPS and InSAR data separately, as well as jointly. Figure 13 shows the best fitting afterslip models derived from the GPS data only, as well as from the joint inversion. In both cases afterslip is found to occur downdip of (and next to) the coseismic rupture. The cumulative afterslip  $\sim 700$  days after the main shock is in excess of  $\sim 0.3$  m. Compared to the afterslip model derived using the GPS data alone, the joint GPS/InSAR inversion suggest a more compact slip distribution. Also, the maximum slip in the joint inverse model is closer to the downdip edge of the coseismic rupture, suggesting that addition of InSAR data does improve the model resolution. The preferred model fits the data reasonably well (Figure S9).

#### 4.3.2. Stress-Driven Afterslip

Kinematic inversions indicate that the observed postseismic deformation  $\sim 2$  years following the 2015 Gorkha earthquake can be well explained by an afterslip model with most of the slip occurring at the downdip end of the coseismic rupture. To verify whether the slip amplitude and distribution are consistent with relaxation of coseismic stress changes on a fault plane, we performed a suite of numerical simulations assuming that the evolution of afterslip is governed by the rate and state friction. Simulations were performed using the Fourier domain fictitious body force code RELAX (Barbot & Fialko, 2010). Afterslip was only allowed in areas on a fault that experienced a coseismic increase in the Coulomb stress. The geometry of the fault was the same as the one used in kinematic inversions. Assuming quasi-steady creep, the slip rate on the velocity-strengthening part of the fault can be expressed as (e.g., Barbot et al., 2009; Lapusta et al., 2000; Rice & Ben-Zion, 1996)

$$v = 2v_0 \sinh \frac{\Delta\tau}{a\sigma}, \quad (4)$$

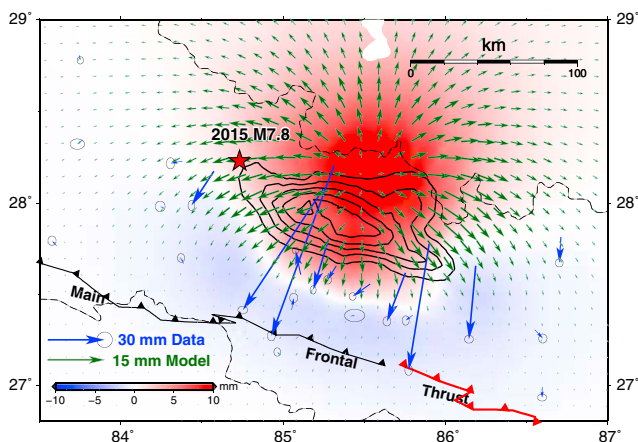


**Figure 12.** A comparison between GPS observations and predicted surface displacements due to poroelastic rebound.

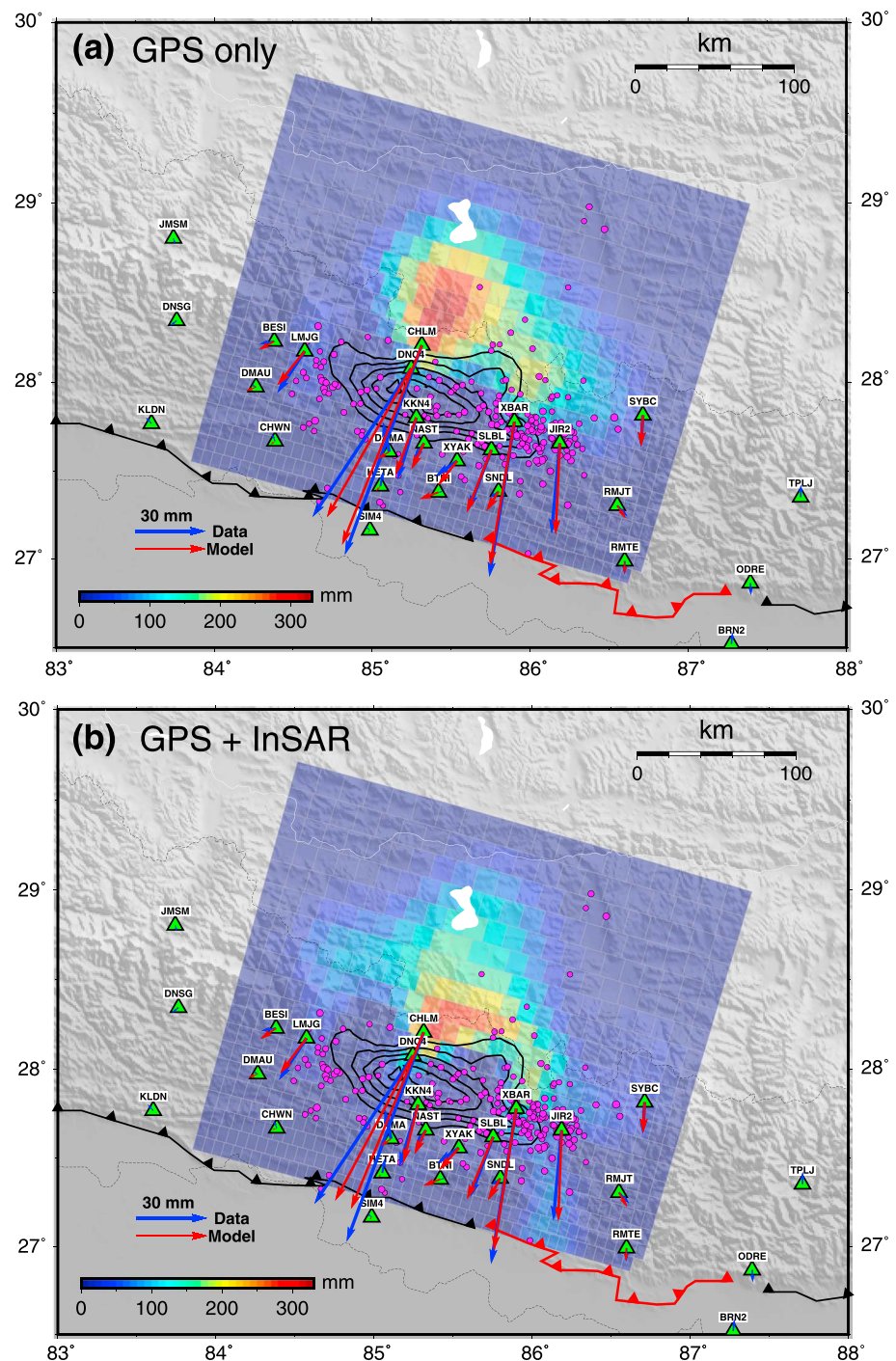


**Figure 13.** Kinematic inversions for afterslip following the 2015 Gorkha earthquake using (a) the horizontal GPS displacements only and (b) both GPS and InSAR LOS displacements. Purple circles denote the  $M4+$  aftershocks.

where  $v_0$  is a reference slip rate,  $\Delta\tau$  is the coseismic shear stress change,  $a$  is the rate and state friction parameter characterizing the direct effect (Dieterich, 1979), and  $\sigma$  is the effective normal stress on a fault. Equation (4) assumes that the evolution effect is negligible, and friction is purely rate dependent.

Stress-driven afterslip models that allowed for creep on a shallow part of the MFT updip of the 2015 rupture produced large horizontal displacements south of the epicenter, which are not observed by the cGPS network (Figure S10). This indicates that the shallow part of the MFT is locked and will release coseismic stress increases

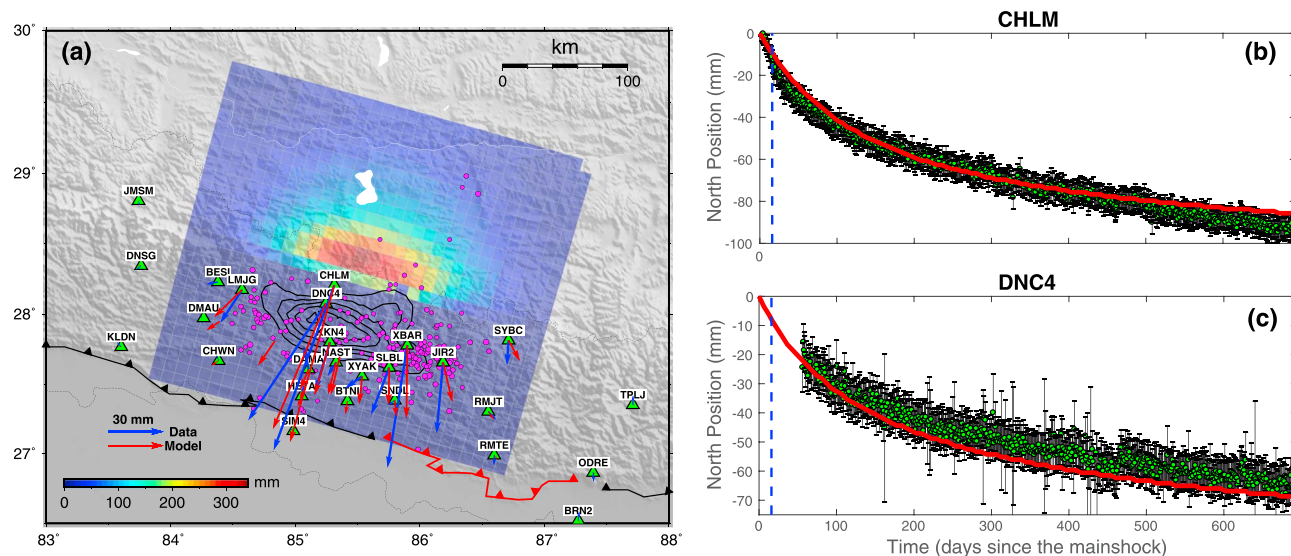


**Figure 14.** A comparison between the GPS observations and stress-driven afterslip models. (a) Cumulative afterslip predicted by the stress-driven afterslip model during the GPS observation period. Observed (green dots with error bars) and predicted (red curve) time series of the north component of the displacement time series at the GPS sites (b) CHLM and (c) DNC4.

due to the Gorkha event in future earthquakes. Thus, we allowed for the velocity-strengthening behavior on a fault plane only below the 2015 rupture. The transition from velocity-weakening to velocity-strengthening behavior is parameterized in our model by the distance from the surface trace of the MFT,  $y_0$ . We performed forward simulations over a wide range of model parameters, including  $v_0$ ,  $a\sigma$  (see equation (4)), and  $y_0$ . Optimal values of these parameters that rendered the best agreement between the model predictions and the GPS data are  $y_0 = 110$  km,  $v_0 = 3.2 \times 10^{-7}$  m/s, and  $a\sigma = 6.5$  MPa. The respective results are shown in Figure 14. Assuming an effective normal stress of  $\sigma = 100$  MPa, this yields an estimate of  $a = 6.5 \times 10^{-2}$ , which is on the order of typical values of the rate dependence parameter ( $a - b \simeq 10^{-3} - 10^{-2}$ ) suggested by laboratory experiments (Marone, 1998; Mitchell et al., 2016). There is a relatively poor agreement between the data and the model predictions between the eastern tip of the 2015 rupture and the  $M_w 7.3$  aftershock (e.g., at the cGPS sites JIR2 and XBAR). While the model shown in Figure 14 is not a result of a formal inversion, a local misfit may be indicative of the along-strike variations in the fault geometry or frictional properties (in particular, the depth of transition from velocity-weakening to velocity-strengthening friction) or some combination of both. Overall, a good qualitative agreement between the model predictions and geodetic observations suggests that the near-field postseismic deformation during  $\sim 2$  years after the main shock was dominated by afterslip on the downdip extension of the coseismic rupture, in response to the stress changes imparted by the 2015 earthquake and its large aftershocks.

## 5. Discussion

Rheologic properties of the lower crust and upper mantle in an active collision zone such as Tibet are of considerable interest as they bear on a number of tectonic and geodynamic problems. There is a long-standing debate about the mechanisms responsible for uplift and topographic variations in continental orogens. In particular, a weak lower crust was proposed to explain the uplift of wide plateaus in the absence of significant internal shortening (Burov & Watts, 2006; Royden et al., 1997; Zhao & Morgan, 1987). Clark & Royden (2000) suggested that the lateral extrusion of the low-viscosity lower crust is responsible for the outward growth of the Tibetan Plateau and that topographic variations across the plateau margins can be explained by a viscous pressure drop within the lower crustal channel of constant thickness. According to this model, gentle topographic slopes (such as those in the northeast and southeast margins of Tibet) are associated with a relatively low viscosity of channel material in foreland ( $10^{18}$  Pa s), while steep slopes (such as those in Nepal) are due to high viscosity of channel material in foreland ( $10^{21}$  Pa s). The model implicitly assumes very low viscosities in the lower crust beneath much of the Tibetan Plateau ( $10^{16} - 10^{17}$  Pa s) to prevent viscous pressure losses (and the associated elevation changes) in the plateau proper. Results presented in this study indicate that the lower crustal viscosity cannot be low either in the foreland or in the adjacent plateau. In the context of the

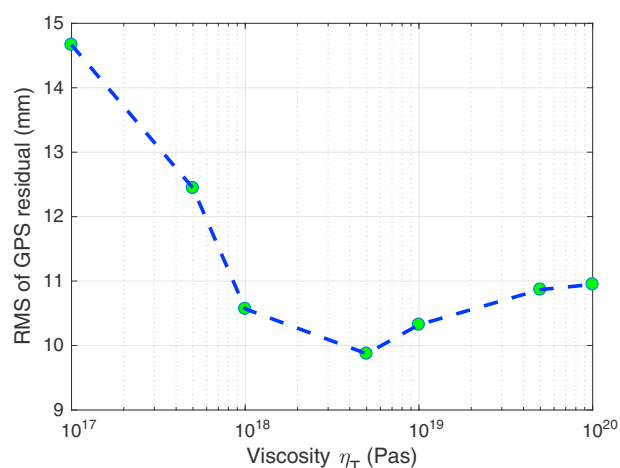


**Figure 15.** RMS of the difference between viscoelastic models and the residual GPS displacements (after subtracting the displacements due to afterslip) as a function of the effective viscosity  $\eta_T$  in the lower crust of southern Tibet.

channel flow model (Clark & Royden, 2000; Royden et al., 1997), the observed postseismic deformation due to the 2015 Gorkha earthquake does not provide useful constraints on the viscosity of the lower crustal material in the foreland, given that the time span of observations is short compared to the expected relaxation time. However, our results do rule out low ( $<10^{18}$  Pa s) viscosities beneath the Tibetan Plateau. Specifically, InSAR LOS and GPS displacements  $\sim 2$  years after the main shock show overall southward and upward motion, while the viscoelastic relaxation models predict northward and downward motion in the epicentral area, regardless of the rheologic structure assumed in the model. For the effective viscosity of  $10^{18}$  Pa s in the lower crust 120 km north of the MFT, the northward displacements predicted by the viscoelastic relaxation models are up to  $\sim 40$  mm during the observation period (Figure 10). The discrepancy between the observations and model predictions would be larger if any viscoelastic relaxation occurred in the foreland (see Figure 8). The amplitude of surface displacements due to viscoelastic relaxation could be reduced by assuming that a transition from strong to weak lower crust occurs farther to the north (larger  $L_T$ , Figure 9). However, this would be inconsistent with the assumption that the topographic slopes are controlled by the viscosity of material in the underlying lower crust (Clark &

Royden, 2000; Royden et al., 1997). Our models assume a simple linear Maxwell rheology. However, note that the predicted spatial patterns of surface displacements would be similar in case of more complex (e.g., the Burgers or the power law) rheologies (Barbot & Fialko, 2010; Huang et al., 2014; Takeuchi & Fialko, 2012, 2013).

As surface displacements due to viscoelastic relaxation and afterslip have opposite signs in the near field of the Gorkha earthquake rupture, an important question is whether some viscoelastic relaxation could be overprinted in the presence of afterslip. To constrain an admissible range of the effective viscosities  $\eta_T$  of the lower crust of southern Tibet, we subtracted the displacements predicted by the preferred stress-driven afterslip model (section 4.3.2) in the limit of full relaxation from the GPS observations and compared the residual displacements to results of forward models of viscoelastic relaxation. Figure 15 shows the misfit of viscoelastic models for different values of  $\eta_T$ . The difference between the residual displacements and model predictions is minimized for the effective viscosities of the lower crust beneath southern Tibet of  $\eta_T > 5 \times 10^{18}$  Pa s. This estimate is based only on the amplitude of horizontal displacements and does not imply that a non-negligible contribution of viscoelastic relaxation in the near field of the 2015 Gorkha event is required by the data. The lower bound on the viscosity might be reduced if one assumes a shallower transition from the velocity-weakening to velocity-strengthening friction (Figure 14a), which will increase the amplitude of afterslip (thereby allowing for a larger viscoelastic contribution). However, we note that models assuming a low-viscosity lower crust beneath high Tibet predict substantial southward movement and uplift on the Tibet side (e.g., north of  $28.5^\circ$  N latitude; see Figure 10). No evidence for such deformation is apparent in the InSAR data presented in this study (Figure 6).

It may be instructive to compare observations and models of postseismic deformation due to the Gorkha earthquake to studies of other large events that occurred in a similar setting. Huang et al. (2014) used InSAR and GPS observations spanning a comparable period ( $<2$  years) after the 2008 Wenchuan (China) earthquake that occurred at the eastern margin of the Tibetan Plateau. They concluded that the data are best explained in terms of viscoelastic relaxation in the lower crust (with the inferred transient viscosity of  $\sim 10^{18}$  Pa s) and upper mantle beneath Tibet; afterslip was argued to be an unlikely mechanism because the best fitting kinematic models required slip at an unreasonably large depth. Because of the challenging surface conditions, the analysis of Huang et al. (2014), however, was based on a rather limited InSAR data set. Wang and Fialko (2014) considered postseismic deformation that occurred over  $\sim 5$  years after the 2005  $M_w$  7.6 Kashmir (Pakistan) at the western end of the Himalayan arc. They found that the near-field deformation was dominated by afterslip on a downdip extension of the earthquake rupture, possibly with a minor contribution from a poroelastic rebound, similar to the results of this study. The lower bound on the effective viscosity of the ductile substrate in the northwestern Himalaya estimated by Wang and Fialko (2014) was  $10^{19}$  Pa s, although their model did not consider possible lateral variations in the rheological structure (e.g., Bendick et al., 2015). Similar values of the effective viscosity were also reported in studies of postseismic transients of large events in central

Tibet (e.g., Ryder et al., 2011, 2014). The effective viscosities in the interior of the Tibetan Plateau constrained by geodetic observations of postseismic transients are thus much higher than the values of  $10^{16}$ – $10^{17}$  Pa s implied by 1-D fluid mechanical models relating the topography variations across the plateau margins to viscosity of the channel material (e.g., Clark & Royden, 2000; Royden et al., 1997). Clark et al. (2005) used 2-D models to relate dynamic pressure due to channel flow around an obstacle to topography variations across the eastern margin of Tibet and inferred the effective viscosity of  $\sim 2 \times 10^{18}$  Pa s in the lower crust beneath the plateau. This estimate is closer to (but still below) the lower bounds suggested by postseismic deformation data. Taken together, results of 1-D and 2-D channel flow models would imply no viscosity contrasts across the plateau margins in areas of gentle topographic slopes (e.g., across the northeast and southeast margins of Tibet), leaving open the question of what controls a transition from the relatively flat plateau to the varying topography in the foreland. It should be noted that the absolute values of viscosity in the context of the channel flow models strongly depend on the assumed channel thickness: a factor of 2 change in the channel thickness would change the viscosity estimates by an order of magnitude. Models of postseismic deformation are less sensitive to the assumed thickness of a low-viscosity layer in the lower crust.

Zhao et al. (2017), based on analysis of GPS data from the Nepal network as well as a few additional sites in southern Tibet over a time period of 1 year after the 2015 Gorkha earthquake, estimated the long-term viscosity beneath the southern Tibet of  $\sim 10^{19}$  Pa s, consistent with the lower bound estimates of this study. The corresponding relaxation time is on the order of 10 years, indicating that viscoelastic relaxation should produce significant surface deformation over the following decade. Studies of postseismic deformation due to megathrust earthquakes in subduction zones reveal signatures of viscoelastic relaxation over decadal time scales (e.g., Hu et al., 2004; Wang et al., 2012). Models of postseismic relaxation due to subduction earthquakes are limited by the data coverage (observations are typically available on the overriding plate and in the far field of earthquake ruptures) and focus on the rheology of the asthenosphere around the subducting slab. The estimated steady state viscosity of the mantle wedge is on the order of  $10^{19}$  Pa s (Hu et al., 2004; Wang et al., 2012). These models also often include a thin low-viscosity layer on the slab interface to improve the data fit in the near field (e.g., Hu et al., 2016; Klein et al., 2016). Such layer may represent either a ductile shear zone (Takeuchi & Fialko, 2012, 2013) or a velocity-strengthening friction interface (“Domain D” in terminology of Lay et al., 2012). Kinematically, contributions from afterslip and ductile flow in a localized shear zone would produce nearly identical deformation patterns at the Earth surface. As there is no evidence for a low-viscosity mantle wedge beneath Himalayas, we did not include such feature in our models.

Our results indicate that the near-field postseismic deformation over  $\sim 2$  years following the 2015 Gorkha earthquake is best explained by afterslip on the MFT with most of the slip concentrated at the downdip end of the coseismic rupture. The inferred afterslip distribution is similar to the results of previous studies that used GPS observations spanning shorter epochs (e.g., Gualandi et al., 2016; Mencin et al., 2016; Zhao et al., 2017). Assuming that the evolution of afterslip is governed by the rate and state friction law, Gualandi et al. (2016) estimated that after full relaxation, the moment release due to afterslip would amount to approximately one third of the seismic moment of the main shock. The moment release estimated from our preferred afterslip model that occurred over  $\sim 2$  years after the main shock (Figure 13b) is  $\sim 6.0 \times 10^{19}$  Nm (assuming the shear modulus of 33 GPa), or  $\sim 10\%$  of the coseismic moment release (Wang & Fialko, 2015). This is in good agreement with results of Zhao et al. (2017) but a factor of  $\sim 2$ – $3$  smaller than the moment release in the limit of full relaxation predicted by Gualandi et al. (2016). Because the rate of afterslip rapidly decays in the first several years following the earthquake, the difference in the aseismic moment release predicted by our models and those of Gualandi et al. (2016) is unlikely to be made up by future afterslip. This difference could in part result from different degrees of smoothing and different fault geometries. It may also be indicative of spatial heterogeneity in frictional properties along the MHT (the analysis of Gualandi et al., 2016 is based on a 1-D spring-slider model).

Our results indicate little or no afterslip on the shallow part of the MHT updip of the 2015 Gorkha rupture. The lack of shallow afterslip indicates velocity-weakening (i.e., seismogenic) behavior of the shallow section of the MFT. This is consistent with models of interseismic deformation that indicate that the MFT is locked all the way from the surface to the seismic/aseismic transition  $\sim 100$  km to the North of the fault trace (e.g., Ader et al., 2012). Hubbard et al. (2016) proposed that the updip propagation of the Gorkha rupture was arrested by a middle-crust fault ramp. Numerical models incorporating the respective complexity in the fault geometry suggest that ruptures of the entire seismogenic zone in the vicinity of the 2015 Gorkha earthquake are indeed possible (Qiu et al., 2016). Sequences of partial ruptures similar to the 2015 Gorkha earthquake



are also reproduced by models assuming a planar fault geometry (Michel et al., 2017). Aftershocks that occurred within months following the main shock are distributed along a relatively narrow band encompassing the coseismic rupture (Adhikari et al., 2015). Available observations and modeling results therefore suggest that the shallow section of the MFT is capable of producing major seismic events. Loading from the 2015 Gorkha earthquake and the accelerated postseismic creep at the bottom of the seismogenic zone (Figure 14a) are bringing the shallow section of the MFT closer to failure.

## 6. Conclusions

The 2015  $M_w$  7.8 Gorkha (Nepal) earthquake occurred along the central Himalayan arc. The epicentral area of the earthquake is characterized by substantial variations in surface elevation and crustal properties. We constructed finite element models to explicitly account for the surface topography and lateral variations in material properties to refine the coseismic slip model of the 2015 Gorkha earthquake and interpret the observed postseismic deformation. Forward models show that surface topography has a relatively minor effect on surface deformation and therefore on results of inverse models. Compared to slip inversions assuming a homogeneous elastic half-space, inversions that use Green functions computed using finite element models that account for both topography and material variations across the Himalaya produce  $\sim 10\%$  more slip at the depth of seismic asperities. Finite fault inversions of the ALOS-2 InSAR observations of the  $M_w$  7.3 (12 May 2015) aftershock suggest that the latter likely occurred on the same fault as the main shock. Neither the main shock nor the aftershock models allow one to distinguish between a planar and a ramp-and-flat fault geometry, although a planar geometry gives rise to a slightly better fit to the data. Postseismic deformation over  $\sim 2$  years after the 2015 Gorkha earthquake is characterized by the southward and upward surface motion in the epicentral area. This pattern is opposite to predictions of viscoelastic relaxation models assuming a low-viscosity channel beneath southern Tibet but is well explained by models of afterslip at the downdip end of the earthquake rupture. The maximum afterslip exceeds 0.3 m over the observation period. The lack of slip on a shallow portion of the MFT during and after the 2015 Gorkha earthquake implies continued seismic hazard in the Kathmandu area. The observed postseismic deformation is inconsistent with models assuming low ( $< 10^{18}$  Pa s) effective viscosity in the lower crust beneath the Tibetan Plateau.

### Acknowledgments

This work was supported by NSF (grant EAR-1547516) and NASA (grant NNX14AQ15G). GPS data used in this study are from a network designed and installed by J.-P. Avouac and colleagues. Raw GPS RINEX files are provided by UNAVCO (last accessed on 15 September 2016). Time series of the station positions are provided by Nevada Geodetic Laboratory (last accessed on 20 April 2017). Sentinel-1 data are provided by the European Space Agency (ESA) through Alaska Satellite Facility (ASF) and UNAVCO. ALOS-2 data are courtesy of the Japanese Space Agency (JAXA). SAR data processing was performed on the Comet cluster at the San Diego Supercomputing Center (SDSC). We thank Yuning Fu for sharing his calculations of the surface deformation at GPS sites using GRACE data. Comments and suggestions by Associate Editor Emma Hill and two anonymous reviewers helped improve this manuscript. Data used in this study are available at <http://igppweb.ucsd.edu/~fialko/data.html>.

### References

- Abaqus/Simulia (2017). A general purpose three-dimensional finite element program. Retrieved from <http://www.3ds.com/products/simulia/overview/>
- Ader, T., Avouac, J.-P., Liu-Zeng, J., Lyon-Caen, H., Bollinger, L., Galetzka, J., ... Flouzat, M. (2012). Convergence rate across the Nepal Himalaya and interseismic coupling on the Main Himalayan Thrust: Implications for seismic hazard. *Journal of Geophysical Research*, *117*, B04403. <https://doi.org/10.1029/2011JB009071>
- Adhikari, L., Gautam, U. P., Koirala, B. P., Bhattarai, M., Kandel, T., Gupta, R. M., ... Bollinger, L. (2015). The aftershock sequence of the 2015 April 25 Gorkha–Nepal earthquake. *Geophysical Journal International*, *203*(3), 2119–2124.
- Avouac, J.-P. (2003). Mountain building, erosion, and the seismic cycle in the Nepal Himalaya. *Advances in Geophysics*, *46*, 1–80. [https://doi.org/10.1016/S0065-2687\(03\)46001-9](https://doi.org/10.1016/S0065-2687(03)46001-9)
- Avouac, J. P. (2007). Dynamic processes in extensional and compressional settings – mountain building: From earthquakes to geological Deformation. In *Treatise on geophysics* (Vol. 6, pp. 377–439). Amsterdam: Elsevier.
- Barbot, S., & Fialko, Y. (2010). A unified continuum representation of post-seismic relaxation mechanisms: Semi-analytic models of afterslip, poroelastic rebound and viscoelastic flow. *Geophysical Journal International*, *182*, 1124–1140. <https://doi.org/10.1111/j.1365-246X.2010.04678.x>
- Barbot, S., Hamiel, Y., & Fialko, Y. (2008). Space geodetic investigation of the coseismic and postseismic deformation due to the 2003  $M_w$  7.2 Altai earthquake: Implications for the local lithospheric rheology. *Journal of Geophysical Research*, *113*, B03403. <https://doi.org/10.1029/2007JB005063>
- Barbot, S., Fialko, Y., & Bock, Y. (2009). Postseismic deformation due to the  $M_w$  6.0 2004 Parkfield earthquake: Stress-driven creep on a fault with spatially variable rate-and-state friction parameters. *Journal of Geophysical Research*, *114*, B07405. <https://doi.org/10.1029/2008JB005748>
- Bendick, R., Khan, S., Bürgmann, R., Jouanne, F., Banerjee, P., Khan, M., & Bilham, R. (2015). Postseismic relaxation in Kashmir and lateral variations in crustal architecture and materials. *Geophysical Research Letters*, *42*, 4375–4383. <https://doi.org/10.1002/2015GL064670>
- Berardino, P., Fornaro, G., Lanari, R., & Sansosti, E. (2002). A new algorithm for surface deformation monitoring based on small baseline differential SAR interferograms. *IEEE Transactions on Geoscience and Remote Sensing*, *40*(11), 2375–2383. <https://doi.org/10.1109/TGRS.2002.803792>
- Bettinelli, P., Avouac, J.-P., Flouzat, M., Bollinger, L., Ramillien, G., Rajaure, S., & Sapkota, S. (2008). Seasonal variations of seismicity and geodetic strain in the Himalaya induced by surface hydrology. *Earth and Planetary Science Letters*, *266*(3–4), 332–344.
- Brocher, T. M. (2005). Empirical relations between elastic wavespeeds and density in the Earth's crust. *Bulletin of the Seismological Society of America*, *95*(6), 2081–2092. <https://doi.org/10.1785/0120050077>
- Burov, E., & Watts, A. (2006). The long-term strength of continental lithosphere: "Jelly sandwich", or "crème brûlée"? *GSA Today*, *16*, 4–10.
- Clark, M. K., & Royden, L. H. (2000). Topographic ooze: Building the eastern margin of Tibet by lower crustal flow. *Geology*, *28*(8), 703–706.
- Clark, M. K., Bush, J. W., & Royden, L. H. (2005). Dynamic topography produced by lower crustal flow against rheological strength heterogeneities bordering the tibetan plateau. *Geophysical Journal International*, *162*(2), 575–590.

- Dieterich, J. H. (1979). Modeling of rock friction 1. Experimental results and constitutive equations. *Journal of Geophysical Research*, *84*, 2161–2168. <https://doi.org/10.1029/JB084iB05p02161>
- Ding, X., Li, Z., Zhu, J., Feng, G., & Long, J. (2008). Atmospheric effects on InSAR measurements and their mitigation. *Sensors*, *8*(9), 5426–5448. <https://doi.org/10.3390/s8095426>
- Elliott, J. R., Jolivet, R., González, P. J., Avouac, J. P., Hollingsworth, J., Searle, M. P., & Stevens, V. L. (2016). Himalayan megathrust geometry and relation to topography revealed by the Gorkha earthquake. *Nature Geoscience*, *9*(2), 174–180. <https://doi.org/10.1038/ngeo2623>
- Fan, W., & Shearer, P. M. (2015). Detailed rupture imaging of the 25 April 2015 Nepal earthquake using teleseismic *P* waves. *Geophysical Research Letters*, *42*, 5744–5752. <https://doi.org/10.1002/2015GL064587>
- Farr, T., & Kobrick, M. (2000). Shuttle Radar Topography Mission produces a wealth of data. *American Geophysical Union EOS*, *81*, 583–585.
- Feng, W., Lindsey, E., Barbot, S., Samsonov, S., Dai, K., Li, P., ... Xu, X. (2016). Source characteristics of the 2015  $M_w$  7.8 Gorkha (Nepal) earthquake and its  $M_w$  7.2 aftershock from space geodesy. *Tectonophysics*, *712*, 747–758. <https://doi.org/10.1016/j.tecto.2016.02.029>
- Ferretti, A., Prati, C., & Rocca, F. (2001). Permanent scatterers in SAR interferometry. *IEEE Transactions on Geoscience and Remote Sensing*, *39*(1), 8–20. <https://doi.org/10.1109/36.898661>
- Fu, Y., & Freymueller, J. T. (2012). Seasonal and long-term vertical deformation in the Nepal Himalaya constrained by GPS and GRACE measurements. *Journal of Geophysical Research*, *117*, B03407. <https://doi.org/10.1029/2011JB008925>
- Gonzalez-Ortega, A., Fialko, Y., Sandwell, D., Alejandro Nava-Pichardo, F., Fletcher, J., Gonzalez-Garcia, J., ... Funning, G. (2014). El Mayor-Cucapah ( $M_w$  7.2) earthquake: Early near-field postseismic deformation from InSAR and GPS observations. *Journal of Geophysical Research: Solid Earth*, *119*, 1482–1497. <https://doi.org/10.1002/2013JB010193>
- Grandin, R., Vallée, M., Satriano, C., Lacassin, R., Klinger, Y., Simoes, M., & Bollinger, L. (2015). Rupture process of the  $M_w=7.9$  2015 Gorkha earthquake (Nepal): Insights into Himalayan megathrust segmentation. *Geophysical Research Letters*, *42*, 8373–8382. <https://doi.org/10.1002/2015GL066044>
- Gualandi, A., Avouac, J.-P., Galetzka, J., Genrich, J. F., Blewitt, G., Adhikari, L. B., ... Liu-Zeng, J. (2016). Pre- and post-seismic deformation related to the 2015,  $M_w$  7.8 Gorkha earthquake, Nepal. *Tectonophysics*, *714–715*, 90–106. <https://doi.org/10.1016/j.tecto.2016.06.014>
- Herring, T., King, R., & McClusky, S. (2015). Introduction to GAMIT/GLOBK.
- Hetland, E. A., & Hager, B. H. (2006). The effects of rheological layering on post-seismic deformation. *Geophysical Journal International*, *166*(1), 277–292.
- Hooper, A., Zebker, H., Segall, P., & Kampes, B. (2004). A new method for measuring deformation on volcanoes and other natural terrains using InSAR persistent scatterers. *Geophysical Research Letters*, *31*, L23611. <https://doi.org/10.1029/2004GL021737>
- Hooper, A., Segall, P., & Zebker, H. (2007). Persistent scatterer interferometric synthetic aperture radar for crustal deformation analysis, with application to Volcán Alcedo, Galápagos. *Journal of Geophysical Research*, *112*, B07407. <https://doi.org/10.1029/2006JB004763>
- Hu, Y., Wang, K., He, J., Klotz, J., & Khazaradze, G. (2004). Three-dimensional viscoelastic finite element model for postseismic deformation of the great 1960 Chile earthquake. *Journal of Geophysical Research*, *109*, B12403. <https://doi.org/10.1029/2004JB003163>
- Hu, Y., Bürgmann, R., Uchida, N., Banerjee, P., & Freymueller, J. T. (2016). Stress-driven relaxation of heterogeneous upper mantle and time-dependent afterslip following the 2011 Tohoku earthquake. *Journal of Geophysical Research: Solid Earth*, *121*, 385–411. <https://doi.org/10.1002/2015JB012508>
- Huang, M.-H., Bürgmann, R., & Freed, A. M. (2014). Probing the lithospheric rheology across the eastern margin of the Tibetan Plateau. *Earth and Planetary Science Letters*, *396*, 88–96. <https://doi.org/10.1016/j.epsl.2014.04.003>
- Hubbard, J., Almeida, R., Foster, A., Sapkota, S. N., Bürgi, P., & Tapponnier, P. (2016). Structural segmentation controlled the 2015  $M_w$  7.8 Gorkha earthquake rupture in Nepal. *Geology*, *44*(8), 639–642. <https://doi.org/10.1130/G38077.1>
- Klein, E., Fleitout, L., Vigny, C., & Garaud, J. D. (2016). Afterslip and viscoelastic relaxation model inferred from the large-scale post-seismic deformation following the 2010  $M_w$  8.8 Maule earthquake (Chile). *Geophysical Journal International*, *205*(3), 1455–1472.
- Lapusta, N., Rice, J., Ben-Zion, Y., & Zheng, G. (2000). Elastodynamic analysis for slow tectonic loading with spontaneous rupture episodes on faults with rate- and state-dependent friction. *Journal of Geophysical Research*, *105*(B10), 23,765–23,789. <https://doi.org/10.1029/2000JB900250>
- Lavé, J., & Avouac, J.-P. (2000). Active folding of fluvial terraces across the Siwaliks Hills, Himalayas of Central Nepal. *Journal of Geophysical Research*, *105*(B3), 5735–5770. <https://doi.org/10.1029/1999JB900292>
- Lay, T., Kanamori, H., Ammon, C. J., Koper, K. D., Hutko, A. R., Ye, L., ... Rushing, T. M. (2012). Depth-varying rupture properties of subduction zone megathrust faults. *Journal of Geophysical Research*, *117*, B04311. <https://doi.org/10.1029/2011JB009133>
- Lindsey, E. O., Natsuaki, R., Xu, X., Shimada, M., Hashimoto, M., Melgar, D., & Sandwell, D. T. (2015). Line-of-sight displacement from ALOS-2 interferometry:  $M_w$  7.8 Gorkha earthquake and  $M_w$  7.3 aftershock. *Geophysical Research Letters*, *42*, 6655–6661. <https://doi.org/10.1002/2015GL065385>
- Marone, C. (1998). Laboratory-derived friction laws and their application to seismic faulting. *Annual Review of Earth and Planetary Sciences*, *26*(1), 643–696. <https://doi.org/10.1146/annurev.earth.26.1.643>
- Masterlark, T. (2003). Finite element model predictions of static deformation from dislocation sources in a subduction zone: Sensitivities to homogeneous, isotropic, Poisson-solid, and half-space assumptions. *Journal of Geophysical Research*, *108*(B11), 2540. <https://doi.org/10.1029/2002JB002296>
- Melosh, H., & Raefsky, A. (1981). A simple and efficient method for introducing faults into finite element computations. *Bulletin of the Seismological Society of America*, *71*(5), 1391–1400.
- Mencin, D., Bendick, R., Upreti, B. N., Adhikari, D. P., Gajurel, A. P., Bhattarai, R. R., ... Bilham, R. (2016). Himalayan strain reservoir inferred from limited afterslip following the Gorkha earthquake. *Nature Geoscience*, *9*, 533–537. <https://doi.org/10.1038/ngeo2734>
- Michel, S., Avouac, J.-P., Lapusta, N., & Jiang, J. (2017). Pulse-like partial ruptures and high-frequency radiation at creeping-locked transition during megathrust earthquakes. *Geophysical Research Letters*, *44*, 8345–8351. <https://doi.org/10.1002/2017GL074725>
- Mitchell, E., Fialko, Y., & Brown, K. M. (2016). Velocity-weakening behavior of Westerly granite at temperature up to 600°C. *Journal of Geophysical Research: Solid Earth*, *121*, 6932–6946. <https://doi.org/10.1029/2012GC004241>
- Monsalve, G., Sheehan, A., Rowe, C., & Rajaure, S. (2008). Seismic structure of the crust and the upper mantle beneath the Himalayas: Evidence for eclogitization of lower crustal rocks in the Indian plate. *Journal of Geophysical Research*, *113*, B08315. <https://doi.org/10.1029/2007JB005424>
- Nábelek, J., Hetényi, G., Vergne, J., Sapkota, S., Kafle, B., Jiang, M., ... Hi-CLIMB Team (2009). Underplating in the Himalaya-Tibet collision zone revealed by the Hi-CLIMB experiment. *Science*, *325*, 1371–1374. <https://doi.org/10.1126/science.1167719>
- Okada, Y. (1985). Surface deformation due to shear and tensile faults in a half-space. *Bulletin of the Seismological Society of America*, *75*(4), 1135–1154.

- Parker, A. L., Biggs, J., Walters, R. J., Ebmeier, S. K., Wright, T. J., Teanby, N. A., & Lu, Z. (2015). Systematic assessment of atmospheric uncertainties for InSAR data at volcanic arcs using large-scale atmospheric models: Application to the Cascade volcanoes, United States. *Remote Sensing of Environment*, *170*, 102–114. <https://doi.org/10.1016/j.rse.2015.09.003>
- Qiu, Q., Hill, E. M., Barbot, S., Hubbard, J., Feng, W., Lindsey, E. O., ... Tapponnier, P. (2016). The mechanism of partial rupture of a locked megathrust: The role of fault morphology. *Geology*, *44*(10), 875–878. <https://doi.org/10.1130/G38178.1>
- Rice, J. R., & Ben-Zion, Y. (1996). Slip complexity in earthquake fault models. *Proceedings of the National Academy of Sciences USA*, *93*, 3811–3818.
- Rousset, B., Barbot, S., Avouac, J.-P., & Hsu, Y.-J. (2012). Postseismic deformation following the 1999 Chi-Chi earthquake, Taiwan: Implication for lower-crust rheology. *Journal of Geophysical Research*, *117*, B12405. <https://doi.org/10.1029/2012JB009571>
- Royden, L. H., Burchfiel, B. C., King, R. W., Wang, E., Chen, Z., Shen, F., & Liu, Y. (1997). Surface deformation and lower crustal flow in eastern Tibet. *Science*, *276*(5313), 788–790. <https://doi.org/10.1126/science.276.5313.788>
- Ryder, I., Bürgmann, R., & Pollitz, F. (2011). Lower crustal relaxation beneath the Tibetan Plateau and Qaidam Basin following the 2001 Kokoxili earthquake. *Geophysical Journal International*, *187*(2), 613–630. <https://doi.org/10.1111/j.1365-246X.2011.05179.x>
- Ryder, I., Wang, H., Bie, L., & Rietbrock, A. (2014). Geodetic imaging of late postseismic lower crustal flow in Tibet. *Earth and Planetary Science Letters*, *404*, 136–143. <https://doi.org/10.1016/j.epsl.2014.07.026>
- Sandwell, D., Mellors, R., Tong, X., Wei, M., & Wessel, P. (2011). Open radar interferometry software for mapping surface deformation. *Eos, Transactions American Geophysical Union*, *92*(28), 234. <https://doi.org/10.1029/2011EO280002>
- Schulte-Pelkum, V., Monsalve, G., Sheehan, A., Pandey, M. R., Sapkota, S., Billham, R., & Wu, F. (2005). Imaging the Indian subcontinent beneath the Himalaya. *Nature*, *435*(7046), 1222–1225. <https://doi.org/10.1038/nature03678>
- Takeuchi, C., & Fialko, Y. (2012). Dynamic models of interseismic deformation and stress transfer from plate motion to continental transform faults. *Journal of Geophysical Research*, *117*, B05403. <https://doi.org/10.1029/2011JB009056>
- Takeuchi, C., & Fialko, Y. (2013). On the effects of thermally weakened ductile shear zones on postseismic deformation. *Journal of Geophysical Research: Solid Earth*, *118*, 6295–6310. <https://doi.org/10.1002/2013JB010215>
- Tong, X., & Schmidt, D. (2016). Active movement of the Cascade landslide complex in Washington from a coherence-based InSAR time series method. *Remote Sensing of Environment*, *186*, 405–415. <https://doi.org/10.1016/j.rse.2016.09.008>
- Tymofeyeva, E., & Fialko, Y. (2015). Mitigation of atmospheric phase delays in InSAR data, with application to the eastern California shear zone. *Journal of Geophysical Research: Solid Earth*, *120*, 5952–5963. <https://doi.org/10.1002/2015JB011886>
- Wang, K., & Fialko, Y. (2014). Space geodetic observations and models of postseismic deformation due to the 2005  $M_{7.6}$  Kashmir (Pakistan) earthquake. *Journal of Geophysical Research: Solid Earth*, *119*, 7306–7318. <https://doi.org/10.1002/2014JB011122>
- Wang, K., & Fialko, Y. (2015). Slip model of the 2015  $M_w$  7.8 Gorkha (Nepal) earthquake from inversions of ALOS-2 and GPS data. *Geophysical Research Letters*, *42*, 7452–7458. <https://doi.org/10.1002/2015GL065201>
- Wang, K., Hu, Y., & He, J. (2012). Deformation cycles of subduction earthquakes in a viscoelastic Earth. *Nature*, *484*(7394), 327–332.
- Wang, R., Lorenzo-Martin, F., & Roth, F. (2006). PSGRN/PSCMP—A new code for calculating co- and post-seismic deformation, geoid and gravity changes based on the viscoelastic-gravitational dislocation theory. *Computers & Geosciences*, *32*(4), 527–541. <https://doi.org/10.1016/j.cageo.2005.08.006>
- Whipple, K. X., Shirzaei, M., Hodges, K. V., & Arrowsmith, J. R. (2016). Active shortening within the Himalayan orogenic wedge implied by the 2015 Gorkha earthquake. *Nature Geoscience*, *9*(9), 711–716. <https://doi.org/10.1038/ngeo2797>
- Xu, X., Sandwell, D. T., Tymofeyeva, E., González-Ortega, A., & Tong, X. (2017). Tectonic and anthropogenic deformation at the Cerro Prieto geothermal step-over revealed by Sentinel-1A InSAR. *IEEE Transactions on Geoscience and Remote Sensing*, *55*(9), 5284–5292. <https://doi.org/10.1109/TGRS.2017.2704593>
- Zhao, B., Bürgmann, R., Wang, D., Tan, K., Du, R., & Zhang, R. (2017). Dominant controls of downdip afterslip and viscous relaxation on the postseismic displacements following the  $M_w$  7.9 Gorkha, Nepal, earthquake. *Journal of Geophysical Research*, *122*, 8376–8401. <https://doi.org/10.1002/2017JB014366>
- Zhao, W.-L., & Morgan, W. J. (1987). Injection of Indian crust into Tibetan lower crust: A two-dimensional finite element model study. *Tectonics*, *6*(4), 489–504. <https://doi.org/10.1029/TC006i004p00489>